Sensors & Actuators: A. Physical 393 (2025) 116779

Contents lists available at ScienceDirect

Sensors and Actuators: A. Physical

journal homepage: www.journals.elsevier.com/sensors-and-actuators-a-physical

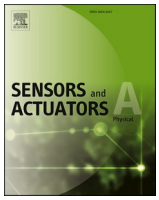

A path toward transferable PEDOT:PSS-based capacitive sensors: Electrical modeling and fabrication

Pedro M.C. Inácio [a,b,*], Rui Guerra [a,b,c], Peter Stallinga [b,d]

[a] CISCA — Cyber-Physical Systems Research Center of Algarve, University of Algarve, Campus Gambelas, Faro 8005-139, Portugal
[b] CEOT — Center for Electronics, Optoelectronics and Telecommunications, University of Algarve, Campus Gambelas, Faro 8005-139, Portugal
[c] Department of Physics, University of Algarve, Campus Gambelas, Faro 8005-139, Portugal
[d] Department of Electronics and Computer Engineering University of Algarve, Campus Gambelas, Faro 8005-139, Portugal

ARTICLE INFO

Keywords:
Capacitive sensors
Transferable PEDOT:PSS electrodes
In-situ electrode fabrication
Self-adhesive sensors
Hydration-sensitive electronics
Flexible electronics
Impedance-based sensing

ABSTRACT

This study presents the development and characterization of a novel transferable capacitive sensor based on poly (3,4-ethylenedioxythiophene):polystyrene sulfonate (PEDOT:PSS) as the primary electrode material. The electrodes were fabricated using an in-situ deposition technique that leverages the self-adhesive, flexible, and highly conductive properties of PEDOT:PSS to enable direct and stable contact with diverse surfaces for continuous, non-invasive hydration measurement. To evaluate their performance, PEDOT:PSS-based sensors were systematically compared with alternative electrode materials—including graphite, silver, gold, and indium tin oxide (ITO)—under controlled humidity conditions. A key innovation in this work is the integration of an ultra-low-cost impedance measurement system, enabling scalable and cost-effective capacitance-based hydration sensing. The study explores sensor fabrication, material characterization, and equivalent circuit modeling, quantifying the contributions of interfacial capacitance and dielectric properties. The results show that PEDOT:PSS electrodes exhibit enhanced hydration sensitivity at the electrode-dielectric interface, confirming that hydration-driven charge transport mechanisms dominate its capacitive response. This unique property allows PEDOT:PSS to detect subtle hydration fluctuations more effectively than conventional electrode materials, making it particularly well-suited for real-time monitoring in wearable electronics, biomedical diagnostics, and environmental sensing. Although physiological validation remains an essential next step, these findings establish a foundation for integrating PEDOT:PSS-based capacitive sensors into bioelectronics, flexible sensing platforms, and environmental monitoring technologies, facilitating the development of cost-effective, non-invasive hydration sensors across multiple fields.

1. Introduction

Advances in electrochemical sensor technology have revolutionized real-time monitoring in various fields, including healthcare, environmental monitoring, and precision agriculture [1,2]. Among these, capacitive sensors have gained much attention due to their non-invasive operation, high sensitivity and adaptability [3–6]. Their ability to detect subtle changes in water balance, ion concentration and physiological parameters has driven innovations in wearable electronics and plant physiology applications [7–12].

Poly(3,4-ethylenedioxythiophene): Polystyrene sulfonate (PEDOT:PSS) has emerged as a strategic material for capacitive sensors due to its high electrical conductivity, mechanical flexibility and biocompatibility [13]. The hydrophilic nature of PEDOT:PSS makes it highly sensitive to moisture fluctuations and enables real-time hydration tracking [14]. These properties have facilitated applications in sweat analysis, epidermal hydration monitoring and environmental sensing [9].

Recent research has extended PEDOT:PSS-based sensors to plant physiology, where monitoring hydration status is critical for assessing water uptake efficiency, transpiration dynamics, and drought stress [15]. Conventional hydration sensors for plants often require mechanical attachment mechanisms such as clamps or adhesives, which can lead to tissue damage, unstable adhesion, and measurement inconsistencies [16–20]. To overcome these limitations, transferable sensors based on PEDOT:PSS — also known as tattoo-like or ultra-deformable sensors — have been developed that adhere seamlessly

* Corresponding author at: CISCA — Cyber-Physical Systems Research Center of Algarve, University of Algarve, Campus Gambelas, Portugal.
E-mail address: pminacio@ualg.pt (P.M.C. Inácio).

https://doi.org/10.1016/j.sna.2025.116779
Received 21 March 2025; Received in revised form 21 May 2025; Accepted 5 June 2025
Available online 6 June 2025

to plant surfaces without additional support structures [21,22].

These ultra-thin, skin-like sensors ensure continuous, non-invasive monitoring of hydration state and improve data accuracy and long-term stability [23,24]. Similar approaches are widely used in biomedical sensing, where tattoo-based PEDOT:PSS electrodes enable reliable electrophysiological signal acquisition [25]. In contrast to conventional electrochemical sweat sensors based on enzymatic or amperometry detection methods, PEDOT:PSS-based hydration sensors offer a label-free, fast, and scalable alternative [9].

A significant challenge in real-time capacitance-based hydration monitoring is the accessibility and cost of impedance measurement systems. Conventional impedance analyzers are often expensive and complex, limiting their use in resource-constrained environments [26]. To overcome this limitation, this study employs an ultra-low-cost capacitance measurement system based on an ATmega328P microcontroller, enabling scalable sensor characterization at minimal cost. While not a primary novelty, this system is a critical enabler for validating the proposed PEDOT:PSS-based sensor technologies in a low-cost and accessible framework [26–34].

Building on these advances, this study presents the development, fabrication, and evaluation of a PEDOT:PSS-based transferable capacitive sensor for real-time hydration monitoring. The proposed sensor integrates a low-cost platform for impedance measurement. It leverages the self-adhesive, flexible, and highly conductive properties of PEDOT:PSS to enable non-invasive and stable sensing. A systematic comparison with alternative electrode materials—including graphite, silver, gold, and indium tin oxide (ITO)—was conducted to assess performance under controlled humidity conditions. Furthermore, an equivalent circuit model was developed to quantify interfacial and dielectric capacitance contributions, providing a framework for optimizing sensor response across different materials.

The results of this study demonstrate that PEDOT:PSS-based sensors offer a versatile platform for capacitive sensing in biomedical diagnostics, wearable hydration monitoring, and environmental sensing applications. By addressing the challenges of sensor adhesion, hydration sensitivity, and scalable fabrication, this work paves the way for integrating PEDOT:PSS electrodes into next-generation flexible electronics, with potential applications in precision agriculture, wearable health monitoring, and environmental surveillance.

2. Materials and methods

2.1. Fabrication of capacitive sensors

The capacitive sensors were fabricated by depositing electrodes made from various conductive materials—graphite, silver, PEDOT:PSS, gold, and indium tin oxide (ITO)—onto cellulose acetate (CA) sheets of varying thicknesses (22, 36, 50, and 75 µm). The CA sheets are dielectric substrates, while the electrodes define the capacitive structure. The fabrication followed a standardized process involving shadow mask preparation, material deposition, drying, and encapsulation when necessary. Depending on the material, electrode integration was performed via direct deposition, transfer techniques, or mechanical fixation.

The selection of CA was motivated not only by practical constraints, such as affordability and commercial availability in well-defined thicknesses, but also by its favorable mechanical flexibility and dielectric stability. This versatility enabled consistent integration across fabrication strategies for different electrodes without requiring adhesives or surface treatments.

Appendices A to F provide details on the fabrication protocols for each electrode material, including deposition methods, post-processing,

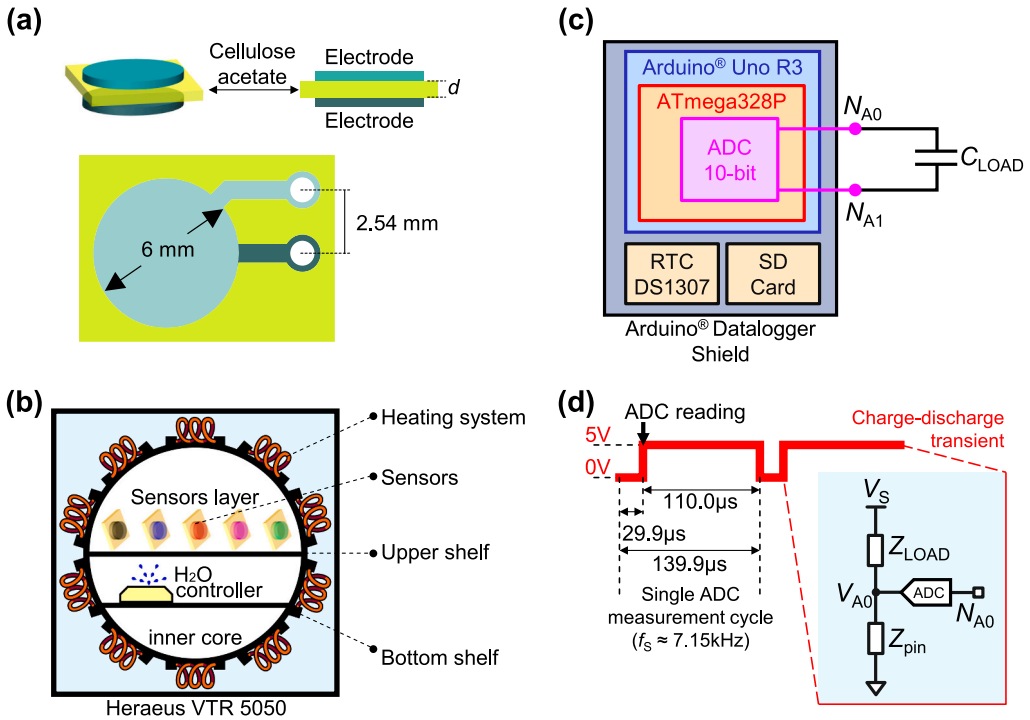

Fig. 1. Experimental setup and measurement system. (a) Schematic and 3D representation of the capacitive sensor's structure. (b) A sectional view of the Heraeus VTR 5050 vacuum oven, highlighting the manifold heating system and the two available shelf positions used for experimental placement. (c) Block diagram of the measurement system showing how each capacitive sensor interfaces with an Arduino® Uno R3 board using the ATmega328P microcontroller and a datalogger shield (RTC DS1307 and SD card) for synchronized acquisition and storage. (d) Schematic representation of the capacitance measurement principle using the ATmega328P microcontroller. A charge-discharge transient is induced by applying a 5 V pulse to the sensor electrode. The ADC sampling defines the pulse period. The measurement cycle timing (29.9 µs discharge, 110 µs charge, total 139.9 µs per cycle) reflects the fast acquisition approach used for capacitance estimation. The inset shows the reduced equivalent circuit illustrating the voltage step method used to determine the sensor capacitance (C_{LOAD}) based on the fast acquisition technique [26].

and encapsulation strategies. Each appendix (B to F) includes a photograph of the complete capacitive structure, showing the electrodes deposited on CA sheets. Fig. 1(b) illustrates the schematic design for fabricating the capacitive sensors, presented in 2D and 3D perspectives.

2.2. Experimental protocols

The same sensors were tested in two configurations: first without encapsulation and then with encapsulation. In the thermal sensitivity experiments, the temperature was increased from 27 ℃ to 60 ℃, while in the relative humidity experiments, the sensors were exposed to a controlled relative humidity between 10 % and 84 %. The experimental setup for characterizing capacitive sensors is detailed in Supplementary Materials S1. Fig. 1(b) illustrates the experimental setup, which consists of a Heraeus VTR5050 vacuum oven integrating a heating control system. A piezoelectric ultrasonic humidifier moistened the atmosphere. All sensors were positioned vertically at the same height on the top of the upper shelf layer of the VTR 5050.

Each capacitive sensor was connected to a dedicated Arduino® Uno R3 board using an ATmega328P microcontroller, which measured capacitance based on its internal 10-bit analog-to-digital (ADC) unit. The measurement principle relies on a fast acquisition mode, where the analog input pin samples the voltage immediately following a 5 V excitation pulse. This approach effectively captures the impulse response of the sensor, functioning as a single-shot charge-discharge transient readout. The measurement cycle duration was 139.9 μs, corresponding to an effective sampling rate of approximately 7.15 kHz, as shown in Fig. 1(d). This method has been validated in Inácio et al. [26]. Further technical details on the effective probing frequency and validation of the dielectric constant extraction methodology are discussed in Appendix I.

To enable simultaneous monitoring of 20 capacitive sensors, a dedicated Arduino® Uno R3 microcontroller was assigned to each sensor. This 1:1 allocation ensured parallel data acquisition without multiplexing, maintaining time synchronization and signal integrity across all channels. Although the detailed hardware arrangement is provided in Supplementary Materials S1, a schematic overview of the measurement system is presented in Fig. 1(c).

Another design feature of the sensor layout is the standardized 2.54 mm spacing between the electrode contacts, which matches the typical pitch of standard header pins used in Arduino® prototyping boards. Without soldering or adapters, this ensured straightforward and repeatable electrical connections to each Arduino® Uno R3 via female pin headers. This compatibility simplified the parallel assembly of 20 sensors and contributed to robust signal acquisition and mechanical stability during the tests, as illustrated in Fig. 1(a).

A datalogger shield mounted on each Arduino board—featuring a real-time clock (DS1307) and SD card module—enabled synchronized data acquisition and local storage. This configuration allowed 20 sensors to be monitored simultaneously under identical environmental conditions.[26]

2.3. Bending test and angle determination

To evaluate the mechanical robustness of the PEDOT:PSS-based capacitive sensors under deformation, a bending test was performed using a custom-built fixture. The setup consisted of two vertical pins acting as support points, positioned symmetrically to impose a controlled bending curvature on the flexible sensor structure. The displacement of these pins was adjusted using a threaded rod mechanism, allowing precise and incremental control of the bending curvature. Sensors fabricated on 22 μm-thick CA sheets were selected for these tests due to their superior flexibility.

Two key geometric parameters were measured to quantify the induced bending:

- ***L* (sagitta):** the vertical displacement at the sensor's center caused by bending.
- ***D*:** the horizontal chord length between the two vertical support pins after displacement.

These definitions align with conventional arc geometry, where the bending angle is derived from the sagitta and chord length, ensuring consistent interpretation with standard methods for flexible substrate characterization. Both L and D were measured using a digital caliper with a resolution of 0.01 mm to ensure precision and repeatability. The initial distance between the support pins in the undeformed (flat) configuration was denoted as D_0.

Assuming the deformed sensor approximates a circular arc, the central arc angle (φ) was computed using the following geometric relationship:

$$\varphi = 2 \bullet \arctan\left(\frac{L}{(D_0 - D)/2}\right). \tag{1}$$

Since the deformation of interest corresponds to the local tilt of each sensor side relative to the flat baseline, the effective bending angle (θ) was defined as:

$$\theta = \frac{\varphi}{2}. \tag{2}$$

A schematic illustration of this measurement method is provided in Fig. 9(a), detailing the geometric relationship between the measured parameters and the computed bending angle.

3. Capacitive sensor modeling

The performance of capacitive sensors is primarily governed by the insulating layer's dielectric properties and the electrodes' configuration. To model these interactions, we begin with the classical parallel plate capacitor equation, which describes the dielectric capacitance (C_{base}) as:

$$C_{base} = \frac{\kappa \varepsilon_0 A}{d}. \tag{3}$$

where κ is the material's dielectric constant, ε_0 is the vacuum permittivity (8.854×10^{-12} F/m), A is the electrode overlap area, and d is the dielectric thickness.

However, in practical capacitive sensors, deviations from this ideal behavior arise due to interfacial imperfections, such as air gaps, surface roughness, and imperfect contact between the electrodes and the

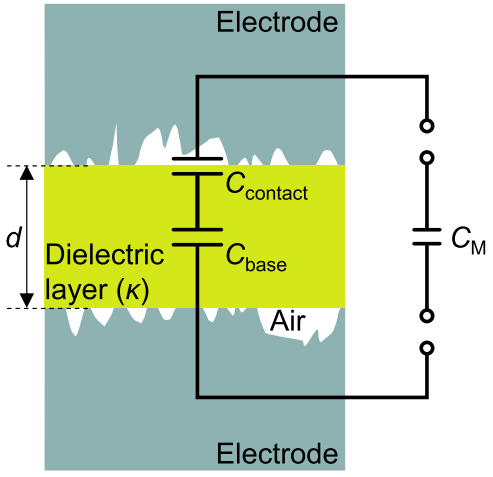

Fig. 2. Equivalent circuit model. Schematic representation of the equivalent circuit model, illustrating the total measured capacitance (C_M) as a combination of interfacial coupling capacitance ($C_{contact}$) and dielectric capacitance (C_{base}) using the series capacitance model.

dielectric. To account for these effects, we introduce an additional component: the interfacial coupling capacitance ($C_{contact}$). Fig. 2 shows the schematic representation of the capacitive sensor interface and the equivalent circuit model.

The total measured capacitance (C_M) can be represented using an equivalent circuit model, where C_{base} and $C_{contact}$ are connected in series:

$$\frac{1}{C_M} = \frac{1}{C_{contact}} + \frac{1}{C_{base}}. \quad (4)$$

This model captures intrinsic dielectric properties and the interfacial contributions to the overall sensor performance. Eq. 4 provides a linear relationship with dielectric thickness:

$$\frac{1}{C_M}(d) = \frac{1}{\kappa\varepsilon_0 A} d + \frac{1}{C_{contact}}. \quad (5)$$

in a plot of $1/C_M$ vs. d, $1/C_{contact}$ represents the intercept, corresponding to the interfacial capacitance, and the slope $1/(\kappa\varepsilon_0 A)$ reflects the material's dielectric properties. If κ is known, the model enables the extraction of $C_{contact}$ through linear regression of measurements taken at different thicknesses.

4. Results

4.1. Experimental characterization

To validate the equivalent circuit model, capacitive sensors were fabricated using CA sheets of varying thicknesses (22, 36, 50, and 75 μm) and five electrode materials—graphite, silver, PEDOT:PSS, gold, and ITO. Sensors were monitored over 50 h, with environmental conditions maintained at 26.1 ± 0.3 °C and 9.3 ± 0.1 % relative humidity (RH) (Fig. 3(a)), ensuring that intrinsic material properties primarily influenced sensor responses.

The baseline capacitance (C_0) represents the steady-state capacitance under stable conditions over 50 h. C_0 was calculated as the average capacitance value over the entire time-series data, where transient fluctuations were minimized. The measured capacitance (C_M) was normalized as $C' = C_M / C_0$ to facilitate direct comparisons across different materials and thicknesses. Fig. 3(b–e) presents the time-dependent normalized capacitance (C') for each electrode material and CA thickness. At the beginning of the measurement period, C' values appear higher due to initial stabilization effects, which may be attributed to electrode polarization, residual charge redistribution, or minor adjustments in environmental conditions. However, these effects gradually diminish as the system reaches a steady-state capacitance.

To assess the stability of the sensor responses, noise levels were quantified using the capacitance signals' standard deviation (σ). At the same time, the coefficient of variation ($CV = 100{\cdot}\sigma / C_0$) was computed as a normalized metric for data variability. Fig. 3(f–h) presents bar plots illustrating the extracted values of C_0, σ, and CV across all electrode materials and CA thicknesses. The results show a systematic decrease in C_0 with increasing CA thickness, consistent with theoretical predictions from Eq. 3. Among the electrode materials tested, graphite, silver, and PEDOT:PSS exhibited the highest C_0 values, whereas ITO consistently showed the lowest capacitance. Gold exhibited intermediate behavior.

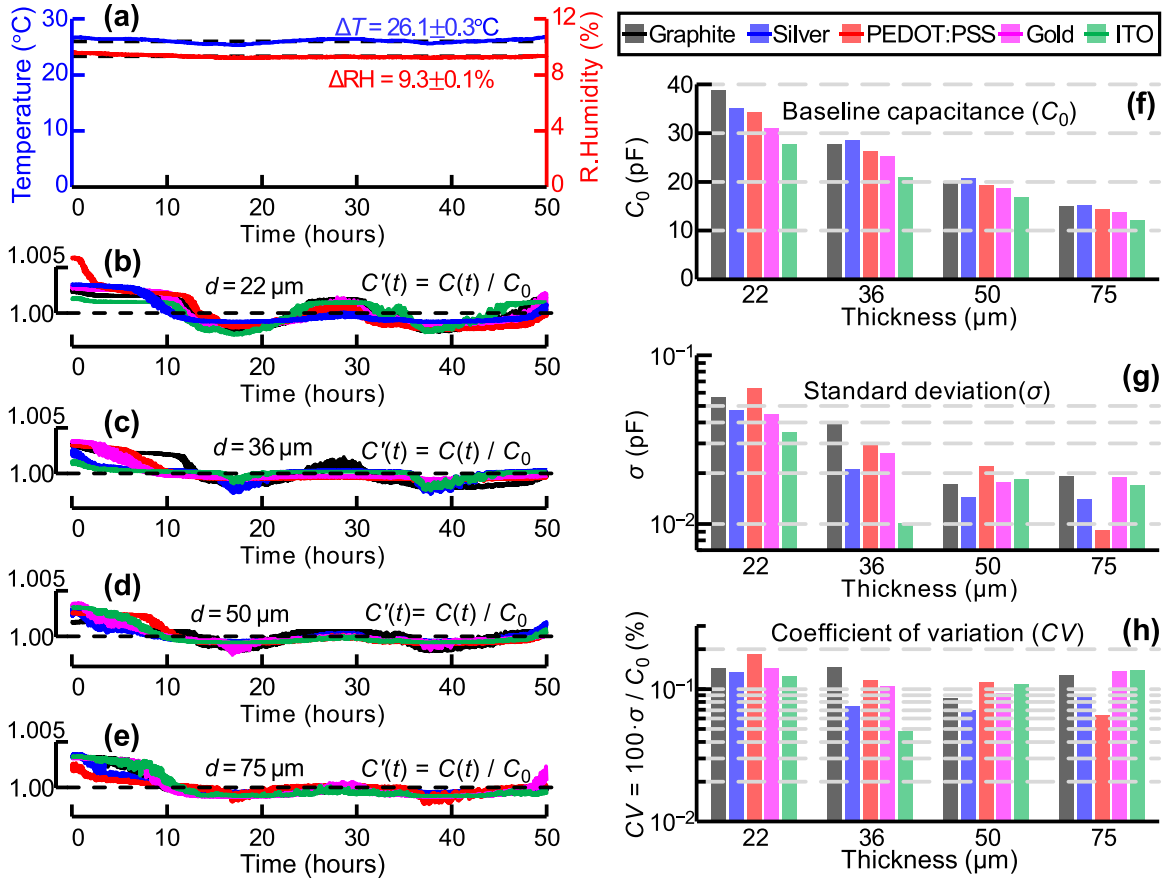

Fig. 3. Time-dependent normalized capacitance (C') for various electrode materials with CA thicknesses of 22, 36, 50, and 75 μm under stable conditions. (a) Recorded temperature (T, °C) and relative humidity (RH, %) over time. (b–e) C' as a function of time, with each panel representing a specific CA thickness. All time-series data are centered around 1, as the dashed line indicates. Instead of axis labels, scale bars are used to represent relative changes. (f) Baseline capacitance (C_0) of each sensor. (g) Standard deviation (σ) of C', indicating sensor noise stability. (h) Coefficient of variation ($CV = 100{\cdot}\sigma / C_0$), providing a normalized measure of the dataset variability.

The numerical values corresponding to the extracted C_0 data shown in Fig. 3(f) are available in Table 1, while the values of σ and *CV* shown in Fig. 3(g–h) are provided in Appendix G, Table G.1.

In addition to capacitance trends, noise stability analysis revealed that the standard deviation (σ) of normalized capacitance (C') generally decreased as CA thickness increased, with only minor fluctuations across different sensor configurations. Notably, PEDOT:PSS exhibited a quasi-linear decrease in noise amplitude (σ) with increasing CA thickness, whereas the other electrodes showed more variable behavior. The *CV* results further confirmed that all electrodes provided stable capacitance measurements. Across all electrode materials, the overall *CV* values remained below 1.5×10^{-3} (< 0.15 %), demonstrating minimal variability and consistent noise performance.

The observed low variability in C_0, as reflected by small standard deviation and *CV* values, demonstrates that the extracted capacitance values are reliable and suitable for computational modeling. These values are the reference dataset for subsequent computational analysis and parameter estimation.

4.2. Computational modeling and fitting

The baseline capacitance values (C_0) extracted from the long-term steady-state data in Fig. 3(f), obtained under stable conditions of 26.1 $\pm$ 0.3 ℃ and 9.3 $\pm$ 0.1 % RH were used as input for computational modeling. Although the experimental characterization provided direct measurements of baseline capacitance (C_0), these values alone do not separate the contributions of interfacial coupling capacitance ($C_{contact}$) and dielectric capacitance (C_{base}). To achieve this decomposition, computational modeling was employed to fit the extracted C_0 values to refine the equivalent circuit model and quantify the capacitance components.

Cellulose acetate (CA) sheets were used as dielectric layers in all sensors to ensure uniform material composition across devices. However, the manufacturer did not provide the precise dielectric constant (κ) of the CA sheets used in sensor fabrication. Literature and manufacturer datasheets report a typical range of $4.5 \leq \kappa \leq 6$ [35–39]. Since the dielectric constant is critical in determining the theoretical capacitance response, accurate estimation was necessary to validate the model. Thus, an iterative least-squares fitting procedure was applied, systematically varying κ within the reported range while minimizing the sum of squared residuals (SSR) between the experimental capacitance measurements (C_0) and the model-predicted equivalent capacitance (C_{eq}).

The optimization procedure follows the linearized equivalent circuit model described by Eq. 5, where the inverse of the measured capacitance is expressed as a function of dielectric thickness. The SSR quantifies the fitting error, ensuring that the selected κ results in the best agreement between the model and experimental data. The total sum of squared residuals (TSSR) was computed as the sum of individual SSR values for each material to evaluate the total fitting error across all electrode materials. The optimal κ was determined by minimizing the TSSR, as shown in Fig. 4(a), yielding $\kappa = 5.22$.

With the optimized κ value, each electrode material's capacitance decomposition was performed to extract $C_{contact}$ and C_{base}. The fitted capacitance curves (C_M) are presented in Fig. 4(b–f), illustrating their dependence on dielectric thickness. The results confirm that $C_{contact}$ contribution systematically decreases as CA thickness increases, while C_{base} becomes the dominant contributor at greater thicknesses, aligning with theoretical expectations.

A confidence interval (CI) analysis was conducted for each electrode material to evaluate the reliability of the fitted capacitance trends. Since the linear regression method assumes a uniform distribution of residuals, the estimated 95 % CIs remain constant along the entire linear fit without thickness dependency. These CIs, shown in Fig. 4(b–f) measure the expected variation in the fitted capacitance values and reinforce the model's robustness. The consistent width of the CIs across all thickness values suggests uniform fitting accuracy, ensuring that the

Table 1
Capacitance components and sensitivity coefficients for each electrode material. C_0 represents the experimentally measured baseline capacitance, while $C_{contact}$ corresponds to the fitted interfacial coupling capacitance. The dielectric capacitance (C_{base}) is constant for each CA thickness and derived from Eq. 3 (values not shown for brevity). Temperature (α_T) and humidity (α_H) sensitivity coefficients correspond to normalized values ($1/C_0 \cdot dC/dT$ and $1/C_0 \cdot dC/dRH$, respectively), extracted from the normalized capacitance curves shown in Figs. 7 and 8 and analyzed in 4.3. These sensitivity coefficients are reported for non-encapsulated (N.E.) and encapsulated (W.E.) configurations. Absolute sensitivities (pF/°C and pF/%RH) can be obtained by multiplying these coefficients by C_0.

Material	$C_{contact}$ (pF)	thickness (μm)			Temperature coefficient								Humidity coefficient					
					$\alpha_T \times 10^{-3}$ (°C^{-1})								$\alpha_H \times 10^{-3}$ (%RH^{-1})					
		C_0 (pF)	22	36	50	75	22		36		50		75		22		36		50		75	
							N.E.	W.E.	N.E.	W.E.	N.E.	W.E.	N.E.	W.E.	N.E.	W.E.	N.E.	W.E.	N.E.	W.E.	N.E.	W.E.
Graphite	106.9	38.8	27.8	20.2	15.1	1.73	1.88	1.67	1.74	2.25	1.24	1.60	2.24	5.81	−0.27	5.24	−0.02	3.27	−0.09	5.19	−0.53
Silver	106.7	35.0	28.5	20.8	15.2	1.61	2.09	1.62	1.63	1.72	1.74	1.77	1.91	5.55	−0.16	−0.06	−0.02	0.72	−0.13	0.24	−0.27
PEDOT:PSS	82.9	34.3	26.2	19.4	14.4	1.69	1.74	1.25	0.97	1.36	0.97	1.26	1.24	9.87	−0.04	8.07	−0.17	6.11	−0.38	3.43	−0.39
Gold	68.5	31.0	25.2	18.7	13.7	1.86	1.22	1.78	1.58	1.98	2.04	1.70	2.15	6.37	−0.09	6.31	−0.11	3.97	−0.23	2.52	−0.01
ITO	46.9	27.8	21.0	16.9	12.1	1.84	1.69	1.23	1.09	1.41	1.92	1.43	1.42	−0.50	−0.01	−0.39	−0.01	−0.27	−0.00	−0.39	−0.02

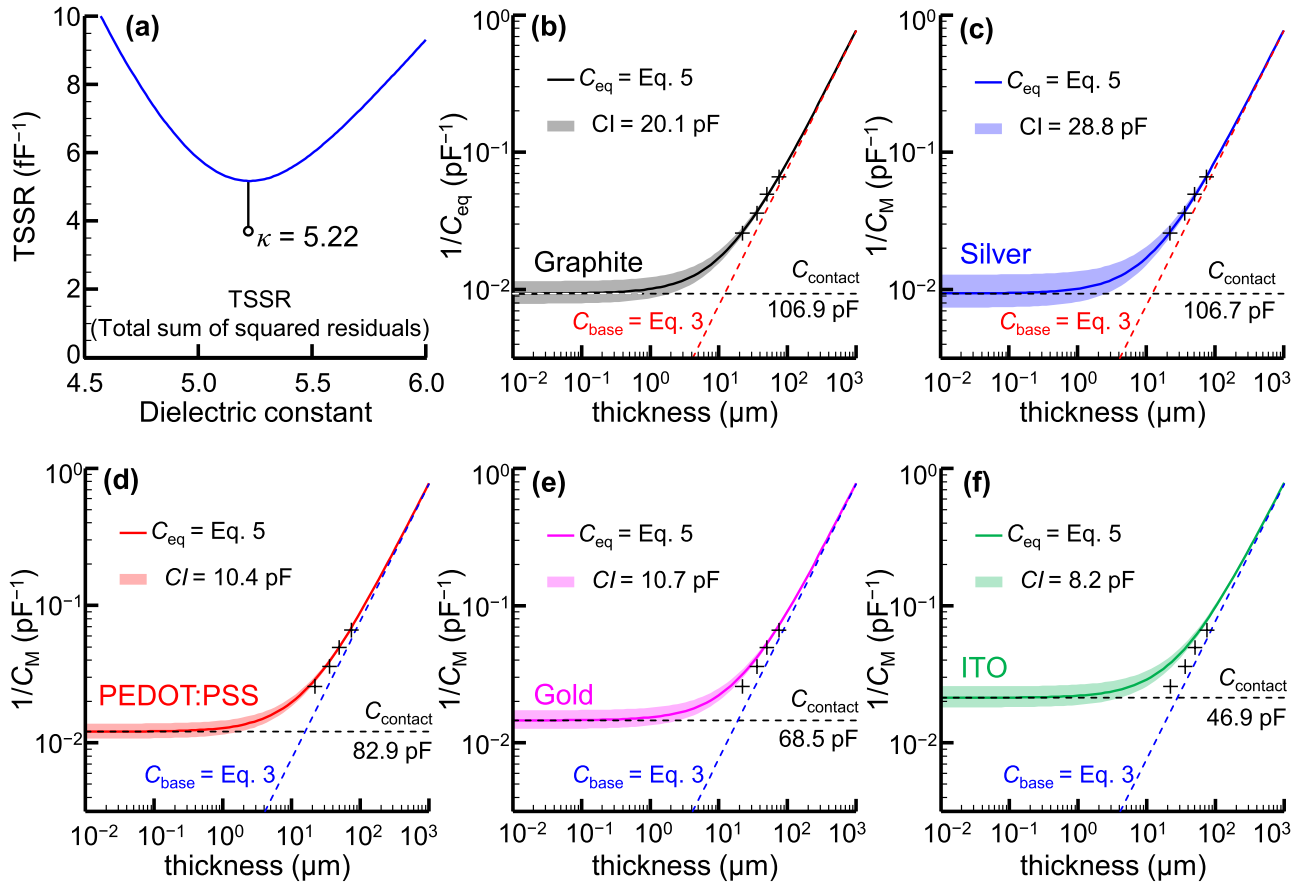

Fig. 4. Computational fitting results for each electrode material. (a) Compound fit error based on the least-squares method for determination of the optimal CA dielectric constant (κ). (b–f) Decomposition of the fitted capacitance (C_{eq}) into interfacial coupling capacitance ($C_{contact}$) and dielectric capacitance (C_{base}) for different electrode materials. The equivalent circuit model (C_{eq} = Eq. 5) predicts systematic trends, with $C_{contact}$ dominating at smaller thicknesses and C_{base} becoming the primary contributor as thickness increases. Shaded regions always represent the confidence interval (*CI*) for the optimal linear fit with $\kappa = 5.22$. All C_0 values used in this model were obtained under controlled environmental conditions of 26.1 ± 0.3 ℃ and 9.3 ± 0.1 % RH, as shown in Fig. 3(a).

extracted capacitance components are statistically meaningful across the entire range of CA thicknesses.

Table 1 summarizes each electrode material's main capacitance model results to facilitate direct comparison. The table includes the experimentally measured baseline capacitance (C_0) for all tested CA thicknesses and the fitted interfacial coupling capacitance ($C_{contact}$). The dielectric capacitance (C_{base}) was assumed to be constant across all electrodes for a given thickness, as determined by Eq. 3. Additionally, temperature (α_T) and humidity (α_H) sensitivity coefficients are provided, derived from the linear response regions discussed in Figs. 7 and 8 and analyzed in 4.3.

The dielectric constant (κ) used in the capacitance model was determined through iterative fitting, minimizing the Total Sum of Squared Residuals (TSSR) across all electrode materials and CA thicknesses. This global fitting approach yielded $\kappa = 5.22$, which best accommodated the diversity of electrode configurations. While independent measurements of κ were performed using a Fluke PM6304 RCL meter, differences in excitation methods and measurement regimes justified using the fitted $\kappa = 5.22$ for modeling purposes. The rationale for this choice, including frequency-dependent effects and method-specific considerations, is discussed in detail in Appendix I.

The final model validation step is presented in Fig. 5, where the experimentally measured C_0 values are plotted alongside the fitted capacitance response across varying CA thicknesses and electrode materials. The strong agreement between the experimental data and the modeled capacitance trends underscores the equivalent circuit model's predictive capability.

To further assess the quality of fit, Fig. 5 presents the coefficient of determination (R^2) for each electrode material, measuring how well the linear model explains the variance in capacitance data. The consistently high R^2 values across all materials confirm that the linearized equivalent circuit model accurately describes capacitance behavior as a function of dielectric thickness, reinforcing its validity in decomposing total capacitance into interfacial ($C_{contact}$) and bulk dielectric (C_{base}) components.

While the computational analysis effectively decomposed the total capacitance into its interfacial and bulk dielectric components, practical applications demand stability under fluctuating environmental conditions. Temperature (T) and relative humidity (RH) variations can significantly impact sensor performance, particularly in applications like hydration monitoring in biological systems. The following section evaluates the sensors' response to environmental changes, highlighting the role of encapsulation in ensuring measurement reliability.

4.3. Sensitivity to environmental conditions

Capacitive hydration sensors must maintain stability under real-world environmental fluctuations, particularly in plant monitoring and wearable sensing applications. Temperature and RH variations can affect dielectric properties and interfacial coupling, altering sensor

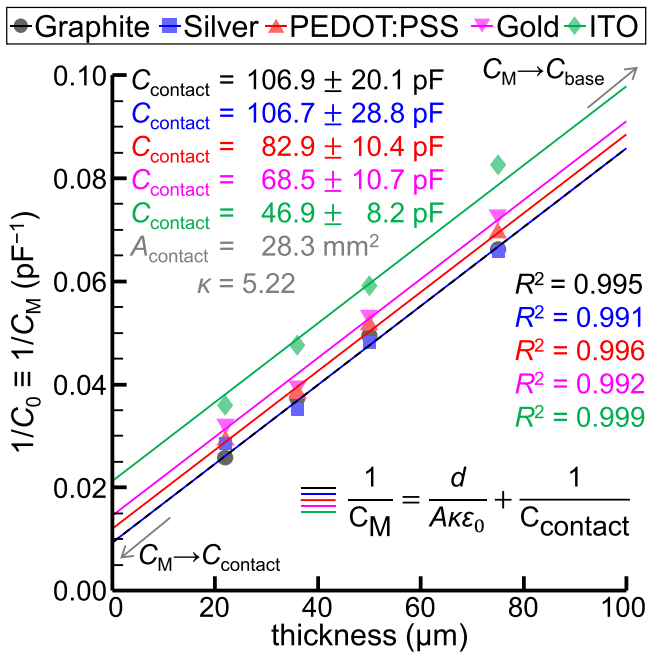

Fig. 5. Computational modeling and fitting. Comparison of experimentally measured baseline capacitance (C_0) values and linear fitted curves across varying CA thicknesses (22, 36, 50, and 75 μm) for different electrode materials, considering the optimal dielectric constant (κ) of 5.22.

capacitance. This section evaluates the sensors' response to environmental changes, comparing non-encapsulated and encapsulated configurations to assess their stability, sensitivity, and reproducibility.

Two key environmental factors were investigated:

- **(i) Temperature sensitivity (α_T)**, analyzed by exposing sensors to a controlled thermal variation from 27°C to 60°C.
- **(ii) Humidity sensitivity (α_H)**, evaluated by exposing sensors to controlled relative humidity (RH) variations from 10 % to 85 %.

Selected regions of interest in the raw data were identified for further analysis, as highlighted Fig. 6(b–e) and Fig. 7(b–e). These figures illustrate the normalized capacitance (C') response during environmental variations for different CA thicknesses. From these data, temperature (α_T) and humidity (α_H) sensitivity coefficients were extracted within the linear response regions, as depicted in Fig. 6(f–m) and Fig. 7 (f–m). Fig. 8 summarizes the extracted α_T and α_H values for different electrode materials and encapsulation conditions, while Table 2 presents the corresponding statistical analysis, including significance tests and effect size metrics. The complete extracted values shown in Fig. 8 are available in Appendix H for further details.

4.3.1. Temperature sensitivity

Temperature dependence was assessed by recording capacitance changes during controlled thermal variations. Fig. 8(a, b) shows the extracted α_T values for different electrode materials under encapsulated (E) and non-encapsulated (N) conditions. A linear relationship between normalized capacitance (C') and temperature was observed during the cooling phase (28°C–43°C), enabling the calculation of α_T as:

$$C'(T) = \alpha_T T + C'_0. \quad (6)$$

where α_T represents the temperature sensitivity coefficient, and C'_0 corresponds to the intercept of the fitted capacitance-temperature curve.

The slope of the C'-vs-T curve within the linear region was used to extract α_T. The extracted α_T values for different electrode materials and CA thicknesses are shown in Fig. 8(a,b) for non-encapsulated and encapsulated sensors.

To evaluate the effects of encapsulation on temperature sensitivity (α_T), Shapiro-Wilk normality tests were performed for each material (Table 2). As all materials followed a normal distribution ($H = 0$), an independent t-test was performed, which gave an overall value of 0.903, confirming that encapsulation had no significant effect on α_T.

Effect size analysis supports this result, with Cliff's Delta ($\delta_T = -0.02$) indicating minimal differences between encapsulated and non-encapsulated sensors. Graphite exhibited the highest α_T of the materials tested, while PEDOT:PSS and ITO showed the lowest values, reflecting differences in the mechanisms of charge transport at the interface.

Fig. 8(c) shows boxplots comparing the α_T distributions for encapsulated (E) and non-encapsulated (N) sensors. The results confirm that encapsulation has no significant effect on temperature sensitivity, consistent with the statistical analysis.

These findings indicate that the temperature sensitivity is primarily determined by electrode-dielectric interactions and not by encapsulation effects. The observed α_T trends highlight the influence of electrode composition, with graphite and silver exhibiting higher temperature sensitivity compared to ITO and PEDOT:PSS.

4.3.2. Relative humidity sensitivity

The influence of relative humidity on sensor performance was evaluated by exposing the sensors to controlled humidity variations between 10 % and 85 %. Fig. 8(d, e) presents the extracted α_H values for different electrode materials under encapsulated and non-encapsulated conditions. A linear relationship was observed during the dehumidification phase (30 %–50 %), enabling the calculation of α_H as:

$$C'(RH) = \alpha_H RH + C'_0. \quad (7)$$

where α_H represents the humidity sensitivity coefficient.

Shapiro-Wilk normality tests were performed to evaluate the statistical effects of encapsulation on α_H (Table 2). Silver (non-encapsulated) did not meet normality ($p = 0.03$, $H = 1$), so a non-parametric Mann-Whitney U (MWU) test had to be used for α_H analysis. The MWU p-value ($p = 0.00029$*) confirms a statistically significant reduction in the α_H value due to encapsulation (where * indicates a statistically significant effect since $p \leq 0.05$).

The effect size analysis provides further insight into this trend. The Cliff's delta for α_H ($\delta_H = 0.67$) shows a substantial shift in RH sensitivity values between encapsulated and non-encapsulated sensors. This result emphasizes that encapsulation significantly reduces the sensors' response to humidity variations, especially for materials such as graphite, PEDOT:PSS, and gold, where $\delta_H = 1.00$. This indicates that all non-encapsulated sensors have α_H values higher than encapsulated sensors.

To illustrate these effects, Fig. 8(f) shows boxplots comparing the α_H distribution between encapsulated and non-encapsulated sensors. The boxplot analysis confirms that encapsulation significantly attenuates the capacitance variations caused by relative humidity, especially for PEDOT:PSS where ion conduction strongly contributes to the sensitivity to relative humidity.

These results suggest hydration plays a crucial role in PEDOT:PSS beyond simple dielectric effects, influencing ion mobility and charge transport properties. 5 (Discussion) further investigates the influence of encapsulation on stabilizing the sensor response under variable humidity conditions.

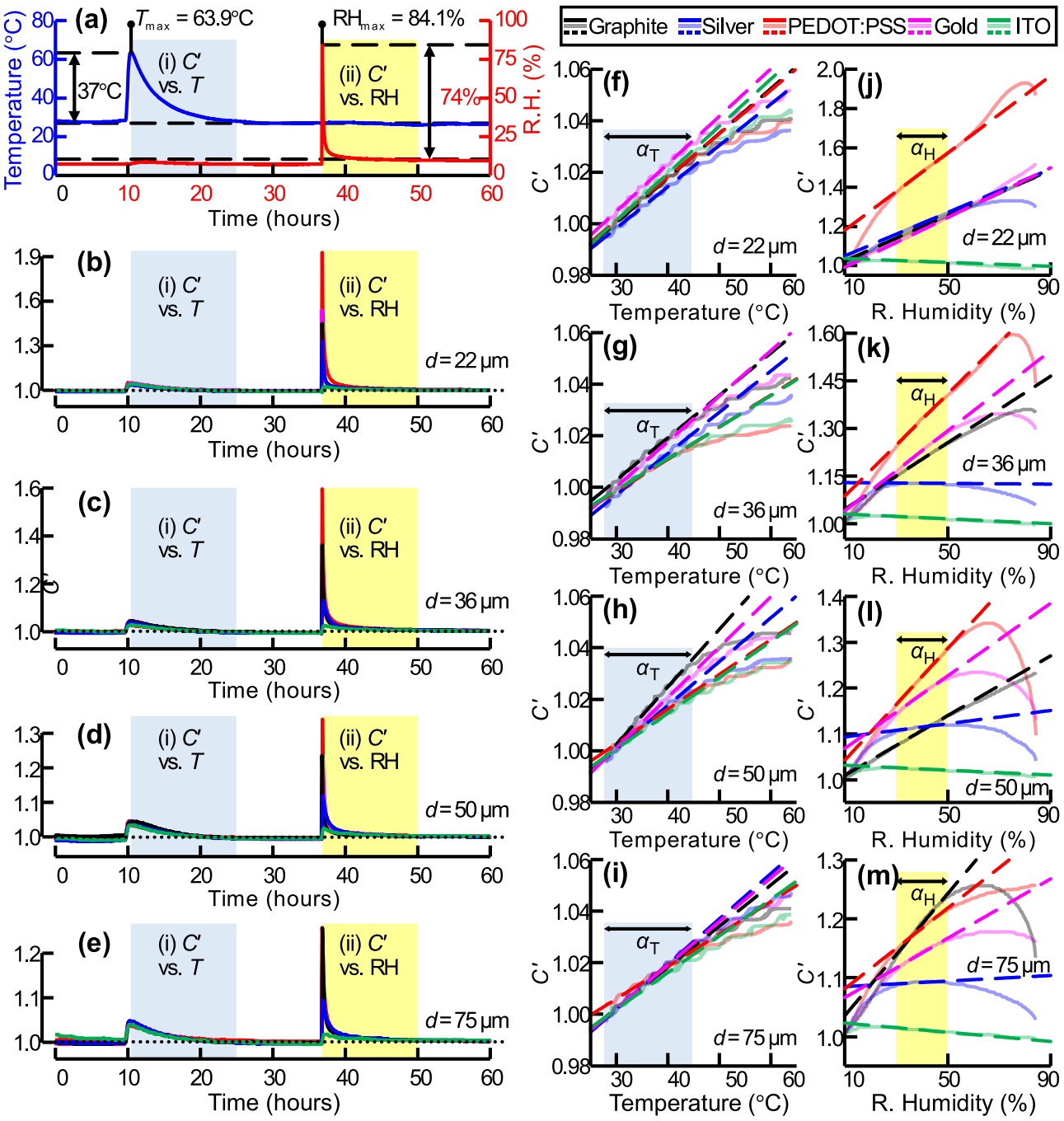

Fig. 6. Temperature and relative humidity (RH) response of capacitive sensors without encapsulation. (a) Five independent sensors recorded the average atmospheric temperature (T, °C) and relative humidity (RH, %). (b–e) Normalized capacitance ($C' = C / C_0$) variations over time for different cellulose acetate (CA) sheet thicknesses (22, 36, 50, and 75 µm), with each panel corresponding to a specific thickness. C_0 represents the baseline capacitance extracted under stable conditions before environmental variations. Each plot shows (i) a response to temperature variation and (ii) RH changes. (f–m) Capacitance decay analysis: (f–i) thermal decay and (j – m) RH decay, focusing on sensor performance within the linear response region. A legend describing the color scheme used in all capacitance charts is provided.

5. Discussion

The results demonstrate that electrode material selection, fabrication techniques, and encapsulation strategies significantly influence the environmental sensitivity of PEDOT:PSS-based capacitive sensors. PEDOT:PSS exhibited the highest RH sensitivity, confirming its strong hydration-driven response. Graphite displayed similar behavior, reinforcing the role of adsorption-based charge transport. Gold and silver showed moderate RH sensitivity, and ITO exhibited minimal dependence on humidity, making it a stable option for temperature-sensitive applications.

Encapsulation effectively stabilized RH-induced fluctuations while preserving temperature sensitivity, indicating that RH sensitivity arises primarily from interfacial hydration effects. In contrast, temperature-driven capacitance variations originate from the electrodes' intrinsic electro-dielectric properties. Additionally, in-situ fabricated PEDOT:PSS electrodes demonstrated strong self-adhesion, forming a stable contact interface that enhances charge transport without needing adhesives or additional structural modifications.

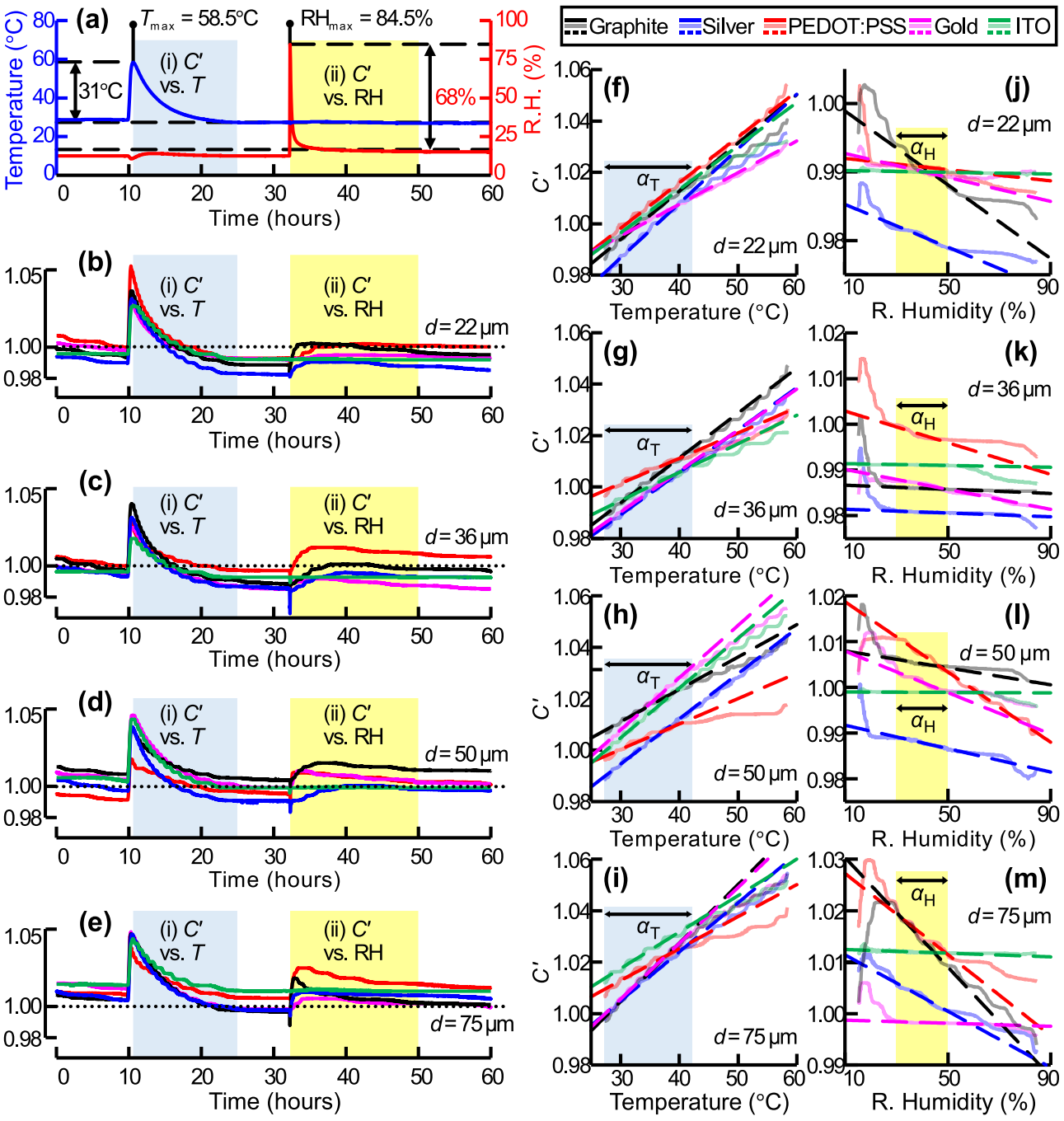

Fig. 7. Temperature and relative humidity (RH) response of capacitive sensors with encapsulation. (a) Five independent sensors recorded the average atmospheric temperature (T, °C) and relative humidity (RH, %). (b–e) Normalized capacitance ($C' = C / C_0$) variations over time for different cellulose acetate (CA) sheet thicknesses (22, 36, 50, and 75 µm), with each panel corresponding to a specific thickness. C_0 represents the baseline capacitance extracted under stable conditions before environmental variations. Each plot shows (i) a response to temperature and (ii) RH changes. (f–m) Capacitance decay analysis: (f–i) thermal decay and (j – m) RH decay, focusing on sensor performance within the linear response region. A legend describing the color scheme used in all capacitance charts is provided.

5.1. *Mechanisms governing environmental sensitivity*

The RH sensitivity of PEDOT:PSS is consistent with the Grotthuss mechanism, where proton transport through hydrogen bonding networks enhances ion mobility, increasing capacitance. This charge transport mechanism has been widely documented in hydrated systems. Wagner and Kliem et al. demonstrated that hydration increases the dielectric constant and interfacial polarization, which in turn affects overall capacitance behavior [40]. Similarly, Bonthuis et al. showed that the dielectric constant of hydrated interfaces is directly related to ion transport, further supporting the role of hydration in PEDOT:PSS charge dynamics [41].

Further evidence comes from Chang and Geise et al., who confirmed that hydrated polymers exhibit strong ion transport effects, reinforcing the influence of water content on electrical response [42]. Additionally, Lee et al. investigated hydration dynamics in ion-gel thin-film

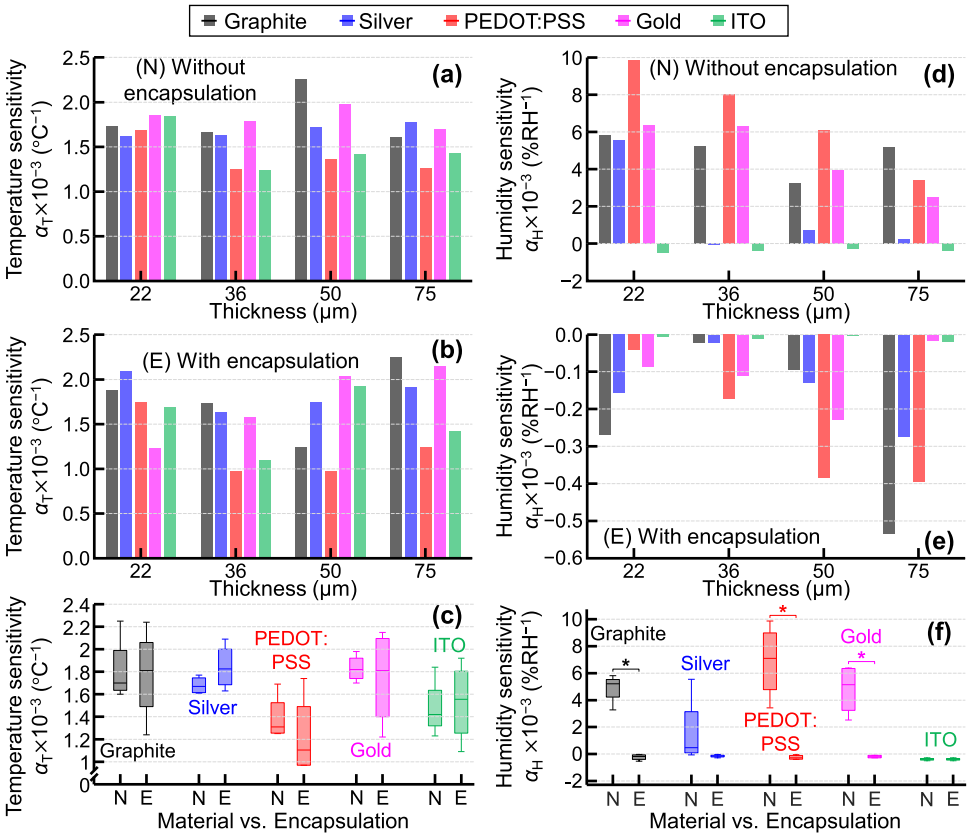

Fig. 8. Temperature and humidity sensitivity of capacitive sensors with and without encapsulation. Panels (a–c) correspond to temperature sensitivity (α_T), and panels (d–f) to humidity sensitivity (α_H). Bar plots (a,b,d,e) show the sensitivity coefficients (α_T in °C^{-1} and α_H in %$^{-1}$) for various electrode materials (graphite, silver, PEDOT:PSS, gold, and ITO) and CA thicknesses (22, 36, 50, and 75 μm), both without encapsulation (a,d) and with encapsulation (b,e). Panels (c,f) show boxplots comparing the distributions of α_T (c) and α_H (f) for non-encapsulated (N) and encapsulated (E) sensors, illustrating the effect of encapsulation on sensitivity variation. The reduction in spread confirms that encapsulation stabilizes α_T and α_H, minimizing fluctuations in sensor response. (*) Indicate statistically significant differences ($p < 0.05$) between encapsulated and non-encapsulated conditions, confirming that encapsulation stabilizes α_T and α_H by reducing variability in sensor response.

transistors, concluding that water layers and ion conduction significantly impact capacitance evolution, a finding that aligns well with the behavior observed in this study [43].

The Maxwell-Wagner-Sillars (MWS) interfacial polarization model, described by Samet et al., provides further insight into the observed behavior of PEDOT:PSS electrodes [44]. The MWS effect occurs in heterogeneous materials where charge accumulation at interfaces leads to polarization and affects the dielectric response. In PEDOT:PSS-based capacitive sensors, hydration increases charge mobility, amplifying interfacial polarization effects, which explains the strong RH sensitivity observed. This also supports the hypothesis that hydration-driven charge transport mechanisms dominate the capacitive response, rather than purely electronic effects.

The statistical analysis in 4.3 further confirms that hydration effects extend beyond simple surface adhesion, as demonstrated by the strong RH sensitivity of PEDOT:PSS ($p = 0.002$, $\delta_H = 1.00$). A similar behavior was observed for graphite and gold, which suggests a common adsorption mechanism, likely involving cellulose interactions at the interface. This indicates that interfacial water adsorption plays a critical role in charge modulation, rather than RH sensitivity being dictated solely by the intrinsic ionic nature of the electrode material.

Encapsulation significantly reduced RH sensitivity ($p = 0.00029$), with PEDOT:PSS, graphite, and gold all exhibiting $\delta_H = 1.00$, indicating a strong suppression of humidity-induced capacitance fluctuations. However, encapsulation did not alter temperature sensitivity, reinforcing that temperature-driven capacitance variations originate from intrinsic electro-dielectric interactions rather than environmental effects.

Beyond the influence of hydration, the results also reveal material-dependent temperature sensitivity (α_T), suggesting that distinct charge transport mechanisms govern the thermal response of the tested materials. Unlike RH sensitivity, which is strongly linked to interfacial hydration, α_T remained unaffected by encapsulation, indicating that temperature-driven capacitance variations arise from intrinsic electro-dielectric properties rather than external environmental factors.

The Variable Range Hopping (VRH) model describes temperature-dependent charge transport in PEDOT:PSS, where thermally activated hopping dominates at higher temperatures [45]. Additionally, Schottky barrier modifications and interface state changes contribute to nonlinear capacitance variations under thermal fluctuations [46].

Temperature-induced changes in dielectric permittivity further explain the observed capacitance variations. A capacitive sensor model developed by Hampson and Dobie et al. demonstrated that temperature-dependent permittivity shifts dominate capacitance variations, reinforcing that thermal effects in capacitive sensors are primarily dictated by intrinsic material properties rather than environmental influences [47]. Additionally, the metallic-semiconducting behavior of PEDOT:PSS, reported by Park et al., suggests that charge transport pathways

Table 2
Statistical results for encapsulation effects on sensor sensitivity: *p*-values obtained with Shapiro-Wilk, *t*-test, Mann-Whitney *U* test (MWU), and effect sizes obtained with Cliff's delta (δ). * $p \leq 0.05$ indicates a statistically significant effect of encapsulation. *H* values in the Shapiro-Wilk test indicate whether normality is assumed ($H = 0$) or rejected ($H = 1$).

Material	Temperature sensitivity (α_T)				
	Shapiro-Wilk test		Significance test		Cliff's delta (δ_T)
	Non-encapsulated *p*-value (*H*)	Encapsulated *p*-value (*H*)	method	*p*-value	
Graphite	0.09 (0)	0.91 (0)	*t*-test	0.89	−0.12
Silver	0.34 (0)	0.88 (0)	*t*-test	0.18	−0.62
PEDOT:PSS	0.10 (0)	0.18 (0)	*t*-test	0.47	0.50
Gold	0.95 (0)	0.56 (0)	*t*-test	0.72	0.00
ITO	0.41 (0)	0.94 (0)	*t*-test	0.82	−0.12
Overall comparison			*t*-test	0.903	−0.02

Material	Humidity sensitivity (α_H)				
	Shapiro-Wilk test		Significance test		Cliff's delta (δ_H)
	Non-encapsulated *p*-value (*H*)	Encapsulated *p*-value (*H*)	method	*p*-value	
Graphite	0.18 (0)	0.61 (0)	*t*-test	0.0001*	1.00
Silver	0.03 (1)	0.94 (0)	MWU	0.06	0.88
PEDOT:PSS	0.95 (0)	0.31 (0)	*t*-test	0.002*	1.00
Gold	0.28 (0)	0.07 (0)	*t*-test	0.002*	1.00
ITO	0.68 (0)	0.68 (0)	*t*-test	1.00	0.00
Overall comparison			MWU	0.00029*	0.67

influence α_T, explaining material-specific temperature responses [48].

These findings confirm that temperature sensitivity in PEDOT:PSS, graphite, and silver is primarily governed by charge transport mechanisms and dielectric permittivity variations rather than hydration effects. The ability of these self-adhesive materials to provide stable interfacial adhesion without external fixation layers enhances their suitability for scalable and transferable capacitive sensors. Gold also exhibited moderate RH sensitivity but retained stable temperature characteristics, making it another viable alternative for applications where minimizing hydration effects is critical.

In contrast, ITO exhibited minimal RH and temperature sensitivity. Still, this result must be interpreted in the context of its mechanical attachment system, which limits direct comparisons to self-adhesive materials. The observed differences highlight the importance of developing self-adhesive capacitive sensors, where PEDOT:PSS and similar materials offer a more effective and scalable path toward flexible, high-performance sensing applications.

5.2. Material-specific sensor performance

The results highlight the crucial role of electrode self-adhesion and in-situ fabrication in optimizing the performance of capacitive sensors, especially in applications requiring direct measurement of hydration. Unlike conventional electrodes that rely on adhesives or external fixation, in-situ fabricated PEDOT:PSS electrodes naturally adhere to dielectric and organic surfaces, forming a stable and intimate contact interface. This strong interfacial coupling enhances the capacitive response by improving charge transport and hydration sensitivity at the electrode-dielectric interface.

Among the materials tested, PEDOT:PSS exhibited the highest RH sensitivity, highlighting its suitability for applications requiring high hydration sensitivity and strong interfacial coupling. Due to its ionic conductivity, water absorption capacity, and self-adhesion properties, it can detect subtle hydration-induced charge changes at the electrode interface. Graphite showed a similar response, making it a viable alternative due to its adsorption-driven charge transport mechanism. In contrast, gold and silver showed moderate RH sensitivity, likely due to their lower interaction with absorbed water molecules and weaker interfacial polarization effects. ITO showed minimal RH sensitivity, suggesting it is suitable for applications where hydration effects should be minimized, with temperature-stable capacitance measurements being the primary concern.

Encapsulation proved effective in stabilizing the fluctuations caused by humidity, significantly reducing variability and maintaining temperature sensitivity. However, encapsulation is not essential in applications where hydration is measured at the electrode interface, such as plant leaf monitoring. In these cases, the electrode acts as a sensor interface, locally detecting hydration fluctuations and not through ambient humidity. This capability is made possible by the self-adhesive nature of PEDOT:PSS, which allows for stable interfacial sensing without additional adhesives or structural changes.

A bending test was performed to evaluate PEDOT:PSS-based capacitive sensors' mechanical robustness for flexible and wearable applications, as detailed in Section 2.3. Sensors fabricated on 22 μm-thick cellulose acetate (CA) sheets were subjected to controlled deformation using a two-pin bending fixture. The bending angle (θ) was determined based on geometric measurements of the sagitta (*L*) and chord length (*D*) between the support pins, following conventional arc geometry definitions.

The applied deformation was quantified across a bending range up to $\theta = 69^{\circ}$. Capacitance measurements were recorded for each bending step, with boxplots summarizing 100 consecutive measurements per angle. As shown in Fig. 9(c,d), the results demonstrated minimal capacitance variation throughout the bending cycle. Occasional outliers (identified by red crosses) appeared at larger bending angles, reflecting transient fluctuations, but remained statistically negligible. Notably, the bent-to-flat transition exhibited fewer outliers, indicating improved mechanical relaxation and interfacial contact recovery during unloading.

Overall, standard deviations remained below 0.5 pF, confirming that mechanical deformation does not significantly impact the capacitive performance of PEDOT:PSS electrodes. These findings validate the robustness and repeatability of the sensors under bending stress, supporting their application in flexible bioelectronics and wearable hydration monitoring platforms.

The material comparison shows that self-adhesive electrodes provide a robust platform for hydration-sensitive capacitive sensors that do not require adhesives while improving charge transport and environmental stability. PEDOT:PSS's ability to seamlessly integrate with organic and dielectric substrates makes it a leading candidate for scalable and transferable sensing applications in wearable hydration monitoring, bioelectronics, and environmental sensing. This ability to function in direct contact applications leads to new sensor development and implementation opportunities.

Additionally, the dielectric constant κ was cross-validated with direct measurements using a Fluke PM6304, obtaining frequency-dependent values from ~6.0 at 50 Hz to ~5.1 at 100 kHz (Appendix I, Fig. I.1). However, the Fluke's AC measurements capture the steady-state dielectric response under sinusoidal excitation. In contrast, the capacitive sensors in this work operate under transient charge-discharge conditions driven by pulsed excitation. At the estimated effective probing frequency of ~7.15 kHz (corresponding to the measuring pulse of 139.9 μs), the Fluke measured $\kappa \approx 5.47$, slightly higher than the fitted $\kappa = 5.22$. Considering this, the fitted κ was retained as the most representative value for modeling the system's behavior. This decision aligns with

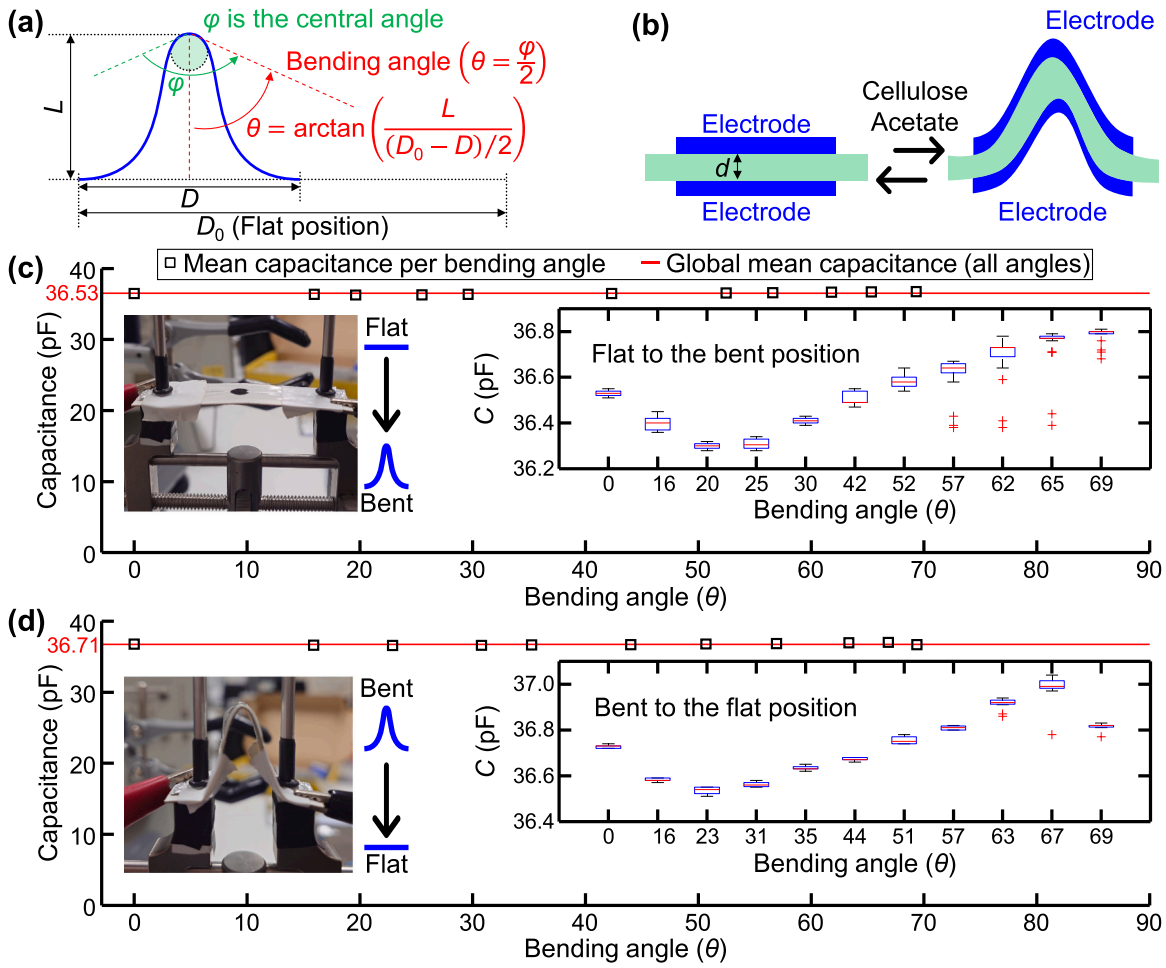

Fig. 9. Effect of mechanical bending on PEDOT:PSS-based capacitive sensors. (a,b) Schematic of the bending angle determination strategy and sensor configuration, with sensors fabricated on 22 μm cellulose acetate (CA) sheets. (c,d) Capacitance variation as a function of bending angle during flat-to-bent (loading) and bent-to-flat (unloading) sequences, showing minimal fluctuation under increasing and decreasing deformation. Each boxplot represents 100 consecutive capacitance measurements per angle, with the red crosses indicating statistical outliers. The boxplots highlight the variation within a narrow capacitance range of approximately 0.6 pF, emphasizing the stability of the sensor under mechanical stress.

literature observations where polymer thin-film dielectrics exhibit frequency-dependent dispersion [49–51], making fitting approaches more suitable for transient-based sensing applications.

5.3. *Influence of dielectric thickness and interfacial effects*

Our results indicate that thinner CA substrates amplify the influence of interfacial polarization mechanisms, enhancing the linear capacitive response in both temperature and humidity sensing. This is because, at reduced dielectric thicknesses, the contribution of the interfacial coupling capacitance ($C_{contact}$) becomes dominant relative to the bulk dielectric capacitance (C_{base}). In other words, the sensor response is increasingly governed by surface-level effects rather than bulk material properties.

This behavior is particularly evident in PEDOT:PSS and graphite-based sensors, which exhibit strong hydration affinity and efficient charge transport at the interface. These characteristics promote extended linearity over broader environmental ranges (notably 30–40 °C and 30–50 % RH), as seen in Figs. 7 and 8. The increased linearity in thinner substrates arises because the electric field penetrates more effectively into the interfacial region, where hydration-driven charge dynamics and Maxwell–Wagner-type polarization effects dominate.

In contrast, noble metals and oxide electrodes (e.g., gold, silver, and ITO) display earlier deviations from linearity, attributable to their weaker interfacial interactions and lower affinity for hydration. This results in a relatively greater influence of bulk dielectric properties, which become more prominent as the CA thickness increases, thereby reducing sensitivity and linear response range.

These findings are consistent with the trends observed in the equivalent circuit modeling (4.2, Fig. 4), where the contribution of $C_{contact}$ decreases with increasing CA thickness. Consequently, optimizing dielectric thickness and electrode material selection is critical when designing capacitive sensors, particularly for applications where interfacial hydration dynamics are key to performance, such as wearable hydration monitoring and plant physiology studies.

5.4. *Implications for sensor design and applications*

The results highlight essential design principles for optimizing capacitive sensors, especially for applications requiring environmental stability and hydration sensitivity. Integrating in-situ fabricated, self-adhesive electrodes such as PEDOT:PSS enables direct contact measurement of hydration, where capacitance changes are caused at the interface and not by the environment.

A significant advantage of self-adhesive electrodes is their ability to form a stable, highly sensitive interface without adhesives or external fixation layers. This property makes them particularly valuable for applications where electrode adhesion and stability are critical for reliable signal acquisition, such as wearable hydration sensors, where stable skin-electrode contact is essential for monitoring the body's water balance, real-time plant water balance monitoring, which allows direct integration into plant tissue without the interference of encapsulation, and biomedical diagnostics, where hydration-sensitive capacitive sensors can be used for continuous physiological monitoring.

Encapsulation continues to be an essential tool for environmental stabilization, especially in applications where humidity fluctuations need to be controlled. However, encapsulation is not always necessary for direct contact applications such as measuring the hydration of plant leaves and wearable bioelectronics. In these cases, the self-adhesive property of PEDOT:PSS provides a natural solution for stable, long-term measurements. The ability to fine-tune the composition of PEDOT:PSS and the methods used to manufacture the electrodes further increases the material's versatility for developing scalable sensors. Using these insights, future sensor designs can integrate PEDOT:PSS-based electrodes into flexible, transferable architectures, expanding their use in next-generation bioelectronic and environmental monitoring technologies.

6. Conclusions

This study highlights the critical role of electrode self-adhesion and in-situ fabrication in optimizing capacitive sensors for hydration-sensitive applications. The results confirm that material selection significantly influences the capacitive response, mainly through hydration-induced charge transport and interfacial interactions. Among the materials tested, PEDOT:PSS exhibited the highest RH sensitivity, highlighting its suitability for direct contact measurement of hydration. The ability of self-adhesive PEDOT:PSS electrodes to detect hydration fluctuations at the electrode-dielectric interface without the need for adhesives or encapsulation expands the potential of capacitive sensors for bioelectronics and environmental monitoring.

A significant achievement of this work is the demonstration that PEDOT:PSS electrodes function as direct contact hydration sensors, providing a stable and highly sensitive interface for detecting hydration-induced capacitance variations. Encapsulation effectively stabilizes humidity-induced fluctuations, but its necessity depends on whether the hydration sensors are driven by the uptake of moisture from the environment or by direct interactions at the interface. The observed hydration-induced charge transport is consistent with the Maxwell-Wagner-Sillars interfacial polarization effect and confirms that charge accumulation at interfaces significantly affects the dielectric response.

The use of a cost-effective capacitance measurement system aligns with the overall goal of developing scalable and accessible hydration sensing platforms, supporting the experimental validation of PEDOT:PSS-based capacitive sensors.

Beyond hydration sensitivity, this study has shown that intrinsic charge transport mechanisms determine temperature-induced capacitance variations, not environmental hydration effects. The variable shifts in dielectric constant provide a solid theoretical framework for the range hopping model and temperature-dependent understanding of these trends and confirm that thermal effects in PEDOT:PSS and other electrode materials arise from intrinsic electro-dielectric properties rather than external moisture effects.

Although these results strongly suggest that ion mobility enhanced by hydration plays a key role in electro-dielectric coupling, further validation is required. Future research will focus on real-time biological sensing applications, particularly plant hydration monitoring, where the self-adhesive properties of PEDOT:PSS enable sensitive and non-invasive detection of ion and hydration fluctuations. In addition, PEDOT:PSS deposition techniques will be optimized to improve uniformity, reproducibility, and interfacial adhesion, and hybrid material compositions will be developed to improve ionic sensitivity and sensor stability.

Another promising research direction is to perform AC impedance measurements with a low-cost impedance system that could provide deeper insight into charge transport at the interface and dielectric response mechanisms. While DC impedance measurements were used in this study, including AC analysis would improve the ability to distinguish between capacitive and resistive contributions and improve sensor performance under dynamic conditions.

These results provide a robust platform for capacitive sensors, facilitating their application in precision agriculture, biomedical diagnostics, and next-generation hydration monitoring technologies. Further exploration of self-adhesive, highly sensitive electrodes will enable the development of biocompatible, flexible, and scalable sensor architectures that support advances in wearable electronics, plant physiology studies, and sustainable sensing technologies.

CRediT authorship contribution statement

Peter Stallinga: Writing – review & editing, Supervision, Resources, Conceptualization. **Rui Guerra:** Writing – review & editing, Supervision, Resources, Project administration, Funding acquisition, Formal analysis, Conceptualization. **Pedro M.C. Inácio:** Writing – original draft, Visualization, Validation, Software, Methodology, Investigation, Formal analysis, Data curation, Conceptualization.

Ethics statements

Not applicable.

Declaration of generative AI and AI-assisted technologies in the writing process

While preparing this work, the author(s) used ChatGPT, Grammarly, and InstaText tools to improve the readability and language of the manuscript. After using this tool, the author(s) reviewed and edited the content as needed and took full responsibility for the content of the published article.

Declaration of Competing Interest

The authors declare that they have no known competing financial interests or personal relationships that could have appeared to influence the work reported in this paper.

Acknowledgments

The FCT—Fundação para a Ciência e a Tecnologia, Portugal—funded this research through the CEOT projects UIDB/00631/2020 CEOT BASE and UIDP/00631/2020 CEOT PROGRAMATICO. This work was also developed under the FEDER/Portugal2020 project NIBAP (ALG-01–0247-FEDER-037303).

Appendix A. — Shadow mask production strategy

Shadow masks (SM) were employed to control the design of all capacitive sensors during fabrication. For solid materials, the masks were made from a 100 μm thick glossy black polyvinyl chloride (PVC) film coated on one side with an adhesive layer (HX20890B, Hexis S.A.S., Frontignan, France). The masks were cut using a Snapmaker Original laser machine with a 1600 mW diode module (Shenzhen Snapmaker Technologies Co., Ltd., Shenzhen, China). Fig. A.1(a) illustrates that the cutting patterns ensured precision and reproducibility. A photograph of a shadow mask attached to a transparent cellulose acetate (CA) sheet (Agar Scientific, Stansted, Essex, UK) is provided in Fig. A.1(b).

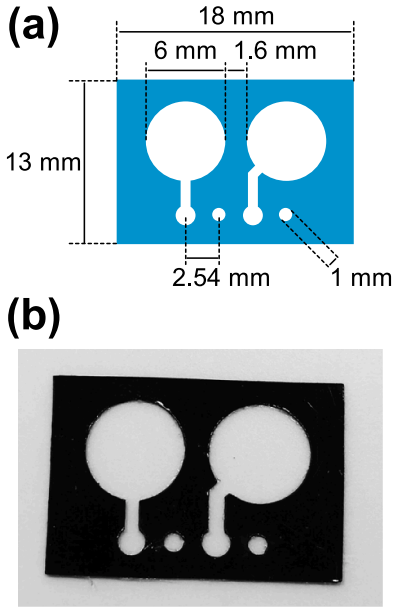

Fig. A.1 Layout of the shadow mask (SM). (a) Design specifications of the SM used to design the electrodes on solid materials. (b) The photograph shows the laser-cut SM made of black PVC film and attached to a transparent cellulose acetate (CA) sheet

Appendix B. — Strategy for fabricating graphite and silver electrodes

The production process for capacitive sensors with graphite and silver electrodes follows a similar methodology and is therefore presented together. The process consists of four steps (A to E), as depicted in Fig. B.1(a).

Step A involves carefully mounting the SM onto the CA sheets. The SM must be handled carefully to ensure proper alignment and overlap on both sides of the CA sheet. Details on the production of SM are provided in Appendix A.

Step B depends on the conductive material used to fill the open areas of the SM/CA structure:

- For graphite electrodes, a water-based, paintable, conductive graphite adhesive with a minimum particle size of 45 μm (Ref. 15411817, Thermo Fisher Scientific, Massachusetts, USA) was used. The graphite material was applied with the brush the manufacturer provided in the bottle cap. For finer details, a small stainless-steel spatula from the laboratory equipment was used while the paint remained wet.
- For silver electrodes, a silver conductive paint (SCP) with 45 % solid content and a particle size of 0.4 −1.0 μm (Electrolube, Leicestershire, UK) was employed. The SCP was deposited using a 1 mL BD syringe fitted with a 25 G cannula tip to ensure precision.

Once the conductive material was applied, **Step C** required the electrodes to dry at room temperature for 1 h on each side. Following this, **Step D** involves carefully removing the SM to prevent electrode damage.

Fig. B.1(b) and (c) show fully assembled capacitive sensors with graphite and silver electrodes, illustrating the results of the described fabrication process.

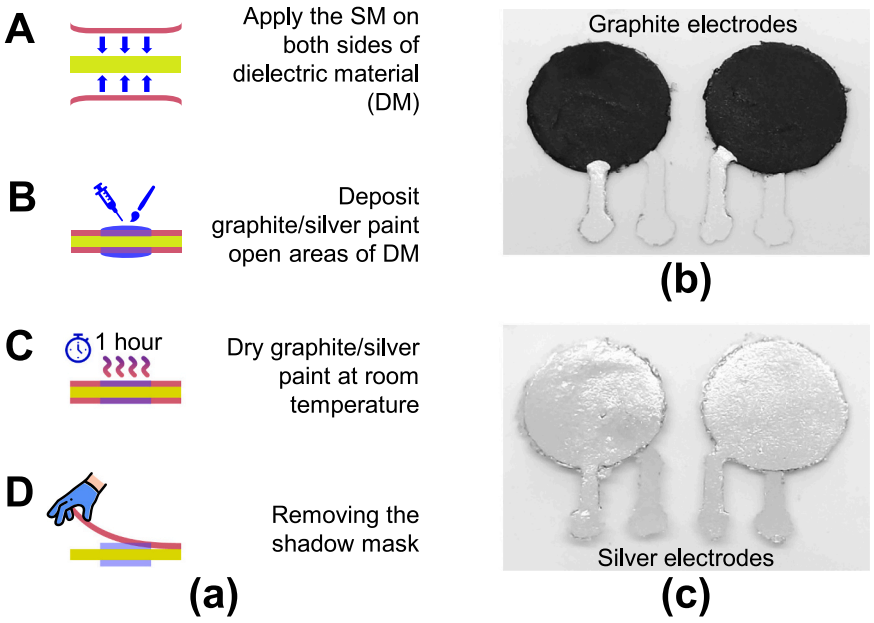

Fig. B.1 Fabrication of graphite and silver electrodes. (a) Step-by-step schematic illustrating the fabrication process. (b,c) Fully assembled capacitive sensor with graphite and silver electrodes on CA sheets.

Appendix C. — Strategy for fabricating PEDOT:PSS tattoo-like electrodes

The fabrication of tattoo-like electrodes from poly(3,4-ethylene dioxythiophene) polystyrene sulfonate (PEDOT:PSS, Clevios™ PH 1000, Ossila Ltd, Sheffield, UK) involved eight sequential steps (A to H), as illustrated in Fig. C.1(a). The detailed process is described below:

Step A: PEDOT:PSS was poured onto decal transfer paper (B06XP7NZ62, Rolurious, Shenzhen, China) to form the electrode layer. The amount of PEDOT:PSS used was sufficient to cover a 4 cm square area (approximately 50 μL/cm^2), allowing the production of four electrodes.

Steps B–D: The following three steps included:

Annealing: The PEDOT:PSS-coated paper was annealed on a hot plate at 60 °C for 2 h.

Chemical Post-Treatment: A thin, uniform layer of dichloroacetic acid (DCA) was applied over the PEDOT:PSS surface to improve electrical conductivity and mechanical ductility by promoting agglomeration of conductive PEDOT grains through the removal of excess PSS content. Excess DCA was removed to minimize drying time.

Second Annealing: The PEDOT:PSS was annealed at 60 °C for 2 h, following the same procedure.

These steps enhanced the electrical, mechanical, and thermoelectric properties of the PEDOT:PSS electrodes [52–55].

Step E: The annealed PEDOT:PSS layer was cut into circular electrodes with a 6 mm diameter using a single-hole punch plier (PF25A001, Rapesco®, Sevenoaks, UK). Each punch produced a single circular electrode.

Step F: The punched PEDOT:PSS electrodes were detached from the decal transfer paper by immersing them in deionized water for approximately 60 s. The water softened the adhesive, enabling the PEDOT:PSS layer to self-detach. If the layer did not self-detach, precision tweezers assisted the process.

Step G: The detached PEDOT:PSS electrodes were transferred onto CA sheets. While wearing gloves, the user gently pressed the moistened PEDOT:PSS layer with a finger to facilitate adhesion to the CA sheet. The process mimicked the application of temporary tattoos, allowing smooth and uniform transfer. Fig. C.1 (b) shows a photograph of dry PEDOT:PSS electrodes adhered to a CA sheet.

Step H: The final step involved assembling the capacitive sensor by integrating the PEDOT:PSS electrodes into the CA/SM structure. This procedure was like the graphite and silver electrode assembly in Appendix B, with adjustments for PEDOT:PSS electrodes. Fig. C.1(c) shows the fully assembled capacitive sensor with PEDOT:PSS electrodes.

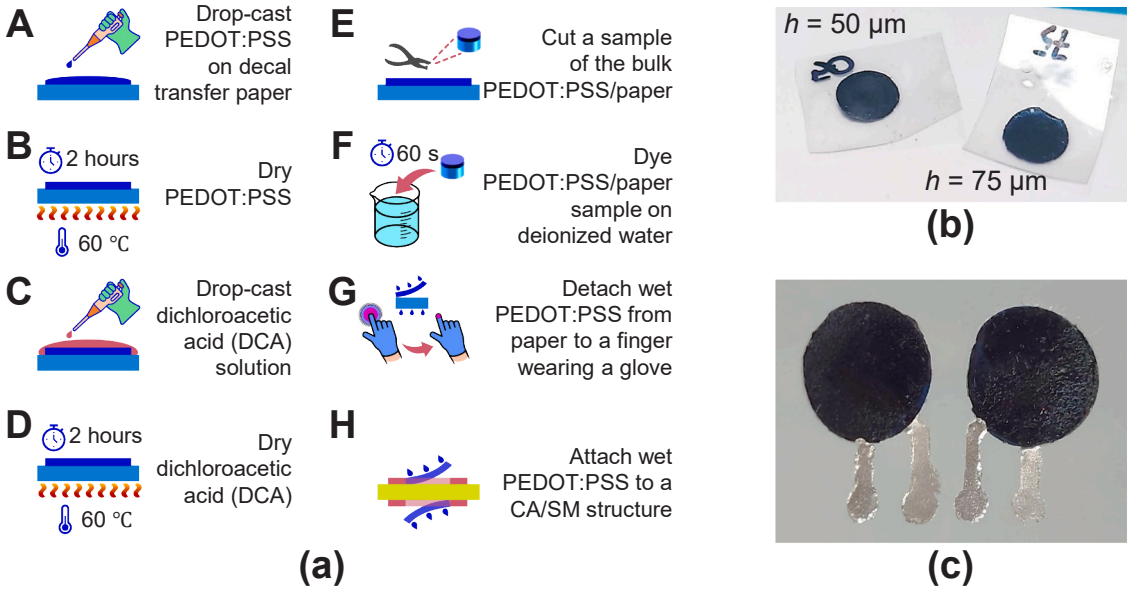

Fig. C.1 Fabrication of PEDOT:PSS tattoo-like electrodes. (a) Step-by-step schematic illustrating the fabrication process. (b,c) Photographs showing PEDOT:PSS electrodes transferred onto CA sheets of various thicknesses and the fully assembled capacitive sensor

Appendix D. — Strategy for fabricating gold electrodes

Fabricating capacitive sensors with gold electrodes involved nine steps (A to J), as depicted in Fig. D.1(a). The gold electrodes were made from 24-carat edible gold leaf (EGL), approximately 0.2–0.4 µm thick (Slofoodgroup LLC, Florida, USA). In its raw form, EGL is supplied as 4.3 × 4.3 cm sheets with protective paper foil on both sides.

Step A: To minimize material wastage and simplify deposition onto solid surfaces, EGL sheets were laser-cut into rectangles measuring 18 mm in length and 13 mm in width. Cutting was performed using a Snapmaker Original laser machine with a 1600 mW diode module (Shenzhen Snapmaker Technologies Co., Ltd., Shenzhen, China). Fig. D.1(b) illustrates the EGL in its original size and as laser-cut pieces.

Steps B–D: Preparing the CA sheets and applying shadow masks (SM).

- **Step B**: Shadow masks were carefully aligned and applied to both sides of the CA sheets. since the shadow masks fabrication strategies are detailed in Appendix A.
- **Steps C and D**: The CA/SM surface was treated with an antistatic coating to facilitate the adhesion of EGL. Vetril Anti-Dust Spray (Bolton Group B. V., Lombardy, Italy), a general-purpose household cleaner, was applied, and excess spray was removed using a microfiber cloth.

Steps E–H: Transfer of the EGL to the CA/SM material.

- **Step E**: Laser-cut EGL pieces were placed in a stable structure and handled in a controlled, unventilated environment. Only the top protective film of the EGL was removed, exposing the adhesive layer. The antistatic-treated CA/SM material was carefully pressed onto the exposed EGL using a gloved finger, ensuring even pressure over the open areas of the shadow mask.
- **Step F**: Excess EGL material outside the electrode pattern was removed with a cotton swab. This step is optional but improves the design's overall precision.
- **Step G**: To address small air pockets near the edges of the shadow mask, a drop of 99 % isopropyl alcohol (IPA) was applied to the electrode areas. The IPA helped settle the EGL material and ensure proper adhesion. Only a minimal amount of IPA was enough to cover the electrode surface.
- **Step H**: After IPA application, the solution evaporated completely within approximately 10 min, ensuring firm adhesion of the EGL to the CA sheet.

Steps I–J: Finalization of the counter electrodes.

- **Step I**: To prepare the counter electrodes, steps C to H were repeated for the opposite side of the sensor.
- **Step J**: The SM were carefully removed, completing the electrode assembly.

Fig. D.1(c) shows a photograph of the assembled sensor with EGL electrodes on a CA sheet.

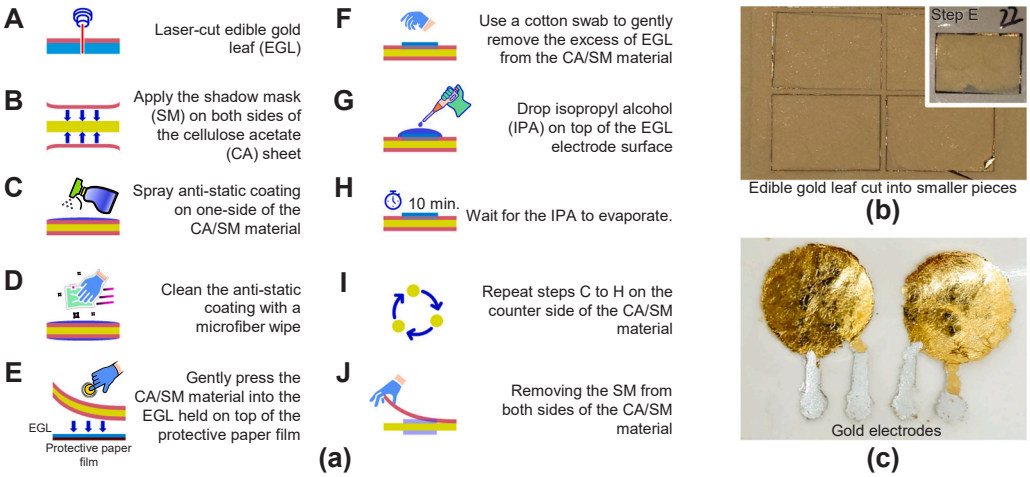

Fig. D.1 Fabrication of gold electrodes. (a) Step-by-step schematic illustrating the fabrication process. (b,c) Photographs showing the edible gold leaf (EGL) in its original size laser cut into smaller parts and the fully assembled sensor

Appendix E. — Strategy for fabricating ITO electrodes

The fabrication of capacitive sensors with indium tin oxide (ITO) electrodes involved eight sequential steps (A–H), as illustrated in Fig. E.1(a). The initial six steps focused on preparing the ITO electrodes and their rigid mechanical support structure, while the final steps involved assembly and integration.

Step A: The rigid structure was used as a 3 mm thick, A3-sized, transparent poly(methyl methacrylate) (PMMA) sheet. A 125 μm thick, A4-sized polyethylene terephthalate (PET) sheet coated on one side with ITO (SMH19H-5, Shenzhen Simihui Electronic Materials Co., Ltd, Shenzhen, China) was selected for the electrodes. The manufacturer-specified sheet resistance of the ITO layer was 5 Ω/□. To attach the ITO/PET structure to the PMMA, a double-sided adhesive layer (3 M™ 300LSE, 3 M Company, Minnesota, USA) was employed.

Steps B–D: The electrodes and PMMA structure were shaped using precision laser cutting (40 W GCC LaserPro Spirit LS, GCC, New Taipei City, Taiwan).

Step B: A laser machine cut the ITO/PET sheet and adhesive layers to form electrode shapes. Minimum laser power and high cutting speeds defined the electrode boundaries, as shown in the dark pink areas in Fig. E.1(b).

Step C: The PMMA material was cut using higher laser power and lower cutting speeds to achieve the desired mechanical support structure, corresponding to the blue areas in Fig. A.1(b). Fig. E.1(c) shows a photograph of the laser-cut materials.

Steps E–F: Assembly of ITO electrodes onto the PMMA parts.

Step E: The two PMMA parts were separated from the larger laser-cut PMMA structure.

Step F: Excess ITO/PET material and adhesive were removed, leaving only the circular ITO electrodes attached to the transparent PMMA, as illustrated in Fig. E.1(d).

Step G: Electrical connections were established between the ITO electrodes and unsheathed, straight pin headers (14.7 mm long, 2.54 mm spacing, available from electronics retailers). Silver conductive paste (SCP, Electrolube, Leicestershire, UK) was applied using a 1 mL BD syringe with a 25 G cannula tip for precision. Approximately 10 μL of a UV-curing acrylic adhesive (KU1053, Krylex®, Georgia, USA) was used to attach the pin headers to the PMMA structure before bonding them to the ITO electrodes with SCP. The adhesive was cured under UV light for 2 min to ensure stability.

Step H: The final assembly of the capacitive sensor involved placing a CA sheet between the upper and lower PMMA parts containing the ITO electrodes. Two pairs of stainless steel M3 screws and nuts were used to press the ITO electrodes and CA sheet together. Fig. E.1(e) shows the assembled sensor with ITO electrodes. For clarity, the M3 screws and nuts are not visible in the figure.

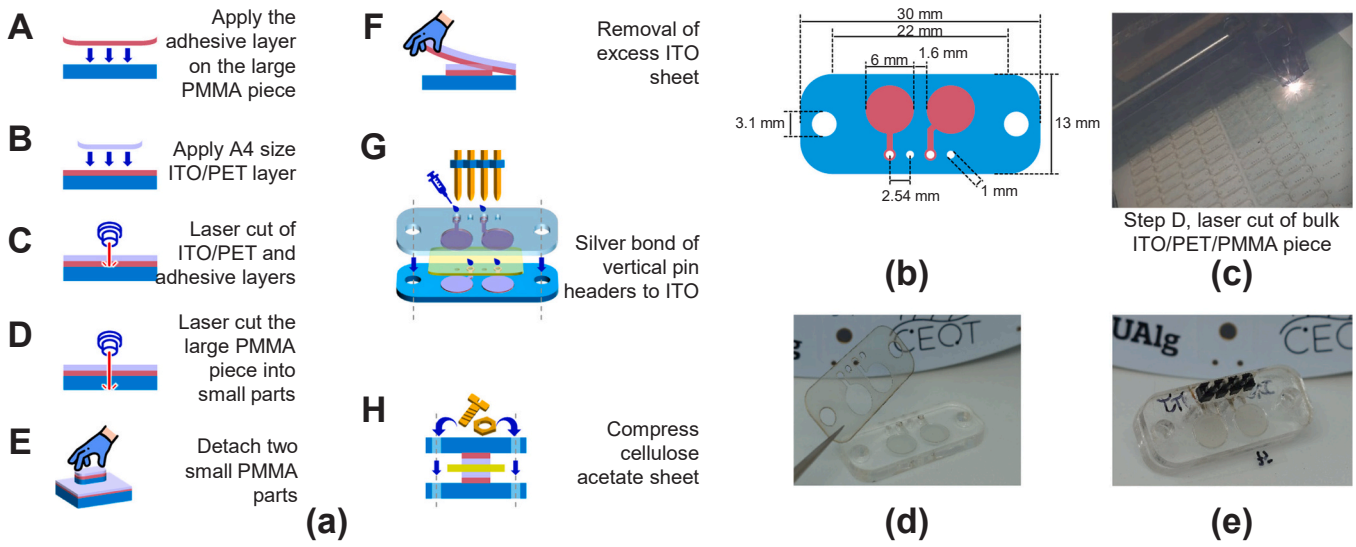

Fig. E.1 Fabrication of ITO electrodes. (a) Step-by-step schematic illustrating the fabrication process. (b) Electrode design for the ITO/PET configuration used in capacitive sensors. (c) The laser cutting process of ITO/PET is attached to the PMMA support structure. (d) A single ITO/PET/PMMA component post-cutting. (e) Fully assembled capacitive sensor with ITO electrodes, demonstrating the integration of mechanical supports for enhanced structural stability

Appendix F. — Encapsulation strategy of capacitive sensors

Capacitive sensors were fabricated with and without encapsulation to improve durability and maintain consistent performance. The encapsulation process employed a one-component, medium-low viscosity ultraviolet (UV)-curing adhesive (KU1053, Krylex®, Alpharetta, GA, USA), selected for its transparency and flexibility upon UV exposure. The adhesive was cured using a 10 W UV LED light operating simultaneously at dual wavelengths of 365 and 395 nm, with a curing time of two minutes.

For sensors with PEDOT:PSS, graphite, silver, and gold electrodes, encapsulation was performed by immersing or coating the electrode and CA structure with the adhesive. This approach ensured uniform coverage, preserving the sensors' mechanical and electrical properties. For ITO electrodes requiring a more delicate procedure, the adhesive was applied with precision between PMMA support structures using a syringe and fine needle. This method minimized material waste while maintaining accuracy.

Appendix G. — Experimental characterization of the sensor model

This appendix presents the detailed data used to support the findings in the main text. The results include tables with the standard deviation (σ) and coefficient of variation (CV) values extracted from the transient capacitance response shown in Fig. 3, which serve as the foundation for subsequent computational analysis.

Table G.1
Extracted standard deviation (σ) and coefficient of variation (CV) values—shown in Fig. 3(g) and (h)—for each sensor as a function of CA sheet thickness

	Cellulose acetate (CA) thickness (μm)							
	22	36	50	75	22	36	50	75
Material	Standard deviation (σ, in fF)				Coefficient of variation (CV)			
Graphite	56.3	40.5	17.2	19.3	1.45×10^{-3}	1.46×10^{-3}	8.51×10^{-4}	1.28×10^{-3}
Silver	47.3	21.1	14.4	14.0	1.35×10^{-3}	7.40×10^{-4}	6.92×10^{-4}	9.21×10^{-4}
PEDOT:PSS	51.2	30.6	22.0	9.2	1.49×10^{-3}	1.17×10^{-3}	1.13×10^{-3}	6.39×10^{-4}
Gold	44.8	26.4	17.6	18.9	1.45×10^{-3}	1.05×10^{-3}	9.41×10^{-4}	1.38×10^{-3}
ITO	35.1	10.1	18.4	16.9	1.26×10^{-3}	4.81×10^{-4}	1.09×10^{-3}	1.40×10^{-3}

Appendix H. — Capacitive sensors thermal and humidity sensitivity analysis

This appendix presents the detailed data used to support the findings in the main text. The results include tables with the thermal sensitivity (α_T) and humidity sensitivity (α_H) coefficients of capacitive sensors, measured for various CA thicknesses (22, 36, 50, and 75 μm) with and without encapsulation. Sensitivity coefficients (α_T and α_H) were extracted for a quantitative assessment using a linear fitting algorithm (MATLAB *polyfit* function, $p = 1$). Main text Fig. 6(f−m) and 7(f−m) show the linear fitting results applied to the experimental data, demonstrating encapsulation's impact on stabilizing sensor responses. Detailed linear fitting parameter values, including intersect values (C'_0) and slopes (α_T and α_H), are provided in Tables H.1 and H.2. This data captures the combined effects of CA thickness, electrode material, and encapsulation on sensor performance, highlighting the importance of optimizing these parameters for precision sensing applications. The extracted α_T and α_H coefficients represent normalized sensitivities, calculated from the normalized capacitance variation ($\Delta C/C_0$) as temperature and humidity functions. Specifically, these coefficients correspond to ($1/C_0 \cdot dC/dT$ and $1/C_0 \cdot dC/dRH$), ensuring that their magnitudes reflect only the inverse dependence on temperature ($℃^{-1}$) and relative humidity ($\%RH^{-1}$), independent of baseline capacitance variations. Absolute sensitivities (expressed in pF/℃ and pF/%RH) can be derived by multiplying these normalized coefficients by the corresponding baseline capacitance (C_0), as detailed in Table 1 of the main text.

Table H.1
Temperature coefficients (α_T) and baseline capacitance (C'_0) for sensors without (N.E.) and with (W.E.) encapsulation, measured over a 15 ℃ range ($\Delta T = 28 - 43$ ℃)

	Thermal sensitivity of the sensors															
	without encapsulation (N.E.)								**with** encapsulation (W.E.)							
thickness (μm)	**22**		**36**		**50**		**75**		**22**		**36**		**50**		**75**	
Material	$\alpha_T \times 10^{-3}$ ($℃^{-1}$)	C'_0	$\alpha_T \times 10^{-3}$ ($℃^{-1}$)	C'_0	$\alpha_T \times 10^{-3}$ ($℃^{-1}$)	C'_0	$\alpha_T \times 10^{-3}$ ($℃^{-1}$)	C'_0	$\alpha_T \times 10^{-3}$ ($℃^{-1}$)	C'_0	$\alpha_T \times 10^{-3}$ ($℃^{-1}$)	C'_0	$\alpha_T \times 10^{-3}$ ($℃^{-1}$)	C'_0	$\alpha_T \times 10^{-3}$ ($℃^{-1}$)	C'_0
Graphite	1.73	0.948	1.67	0.953	2.25	0.935	1.60	0.954	1.88	0.938	1.74	0.942	1.24	0.974	2.24	0.938
Silver	1.61	0.950	1.62	0.948	1.72	0.949	1.77	0.949	2.09	0.924	1.63	0.941	1.74	0.942	1.91	0.948
PEDOT:PSS	1.69	0.951	1.25	0.961	1.36	0.962	1.26	0.968	1.74	0.946	0.97	0.972	0.97	0.971	1.24	0.975
Gold	1.86	0.949	1.78	0.947	1.98	0.942	1.70	0.951	1.22	0.959	1.58	0.943	2.04	0.947	2.15	0.941
ITO	1.84	0.946	1.23	0.962	1.41	0.958	1.43	0.959	1.69	0.946	1.09	0.962	1.92	0.947	1.42	0.975

Table H.2
Humidity coefficients (α_H) and baseline capacitance (C'_0) for sensors without (N.E.) and with (W.E.) encapsulation, measured over a 20 % range ($\Delta RH = 30 - 50$ %)

	Humidity sensitivity of the sensors															
	without encapsulation (N.E.)								**with** encapsulation (W.E.)							
thickness (μm)	**22**		**36**		**50**		**75**		**22**		**36**		**50**		**75**	
Material	$\alpha_H \times 10^{-3}$ ($\%RH^{-1}$)	C'_0	$\alpha_H \times 10^{-3}$ ($\%RH^{-1}$)	C'_0	$\alpha_H \times 10^{-3}$ ($\%RH^{-1}$)	C'_0	$\alpha_H \times 10^{-3}$ ($\%RH^{-1}$)	C'_0	$\alpha_H \times 10^{-3}$ ($\%RH^{-1}$)	C'_0	$\alpha_H \times 10^{-3}$ ($\%RH^{-1}$)	C'_0	$\alpha_H \times 10^{-3}$ ($\%RH^{-1}$)	C'_0	$\alpha_H \times 10^{-3}$ ($\%RH^{-1}$)	C'_0
Graphite	5.81	0.964	5.24	0.992	3.27	0.976	5.19	0.983	−0.27	1.002	−0.02	0.987	−0.09	1.009	−0.53	1.036
Silver	5.55	0.993	−0.06	1.129	0.72	1.086	0.24	1.083	−0.16	0.987	−0.02	0.982	−0.13	0.993	−0.27	1.014
PEDOT:PSS	9.87	1.081	8.07	1.005	6.11	0.981	3.43	1.047	−0.04	0.992	−0.17	1.005	−0.38	1.023	−0.39	1.031
Gold	6.37	0.926	6.31	0.976	3.97	1.028	2.52	1.041	−0.09	0.994	−0.11	0.991	−0.23	1.010	−0.01	0.999
ITO	−0.50	1.040	−0.39	1.033	−0.27	1.034	−0.39	1.027	−0.01	0.990	−0.01	0.991	−0.00	0.999	−0.02	1.013

Appendix I. Validation of dielectric constant extraction methodology

The dielectric constant (κ) used in the capacitance model was obtained by fitting the experimental data through minimization of the Total Sum of Squared Residuals (TSSR) across all electrode materials and cellulose acetate (CA) thicknesses. This global fitting approach yielded $\kappa = 5.22$, providing a representative value that best accommodated the diversity of electrode configurations investigated.

To benchmark this result, an independent measurement of κ was performed using a Fluke PM6304 RCL meter on the same CA dielectric samples (graphite electrodes). The Fluke measurements revealed a frequency-dependent κ, ranging from ~6.0 at 50 Hz to ~5.1 at 100 kHz (Fig. I.1), consistent with the known dispersion behavior of polymer dielectrics.

However, while the Fluke applies a sinusoidal AC voltage probing steady-state response, the ATmega328P-based measurements rely on transient charge-discharge pulses, emphasizing interfacial polarization dynamics. The effective probing frequency of this method was estimated at ~7.15 kHz (corresponding to the measuring pulse of 139.9 μs). The Fluke measured $\kappa \approx 5.47$ at this frequency, slightly higher than the fitted $\kappa = 5.22$.

The differences in measurement principles explain this discrepancy. Conventional LCR meters, as discussed by Feldman et al. (1996) [49] and Sun et al. (2025) [50] may not fully capture the dynamic interfacial effects of thin-film flexible dielectrics. Additionally, Jung et al. (2023) demonstrated that polymer thin films exhibit significant frequency-dependent variations in their dielectric constant, further supporting the need for application-specific measurement approaches [51].

Given these considerations, the fitted $\kappa = 5.22$ was retained as the most representative parameter for the sensors studied, while the Fluke PM6304 measurements served as a valuable consistency check.

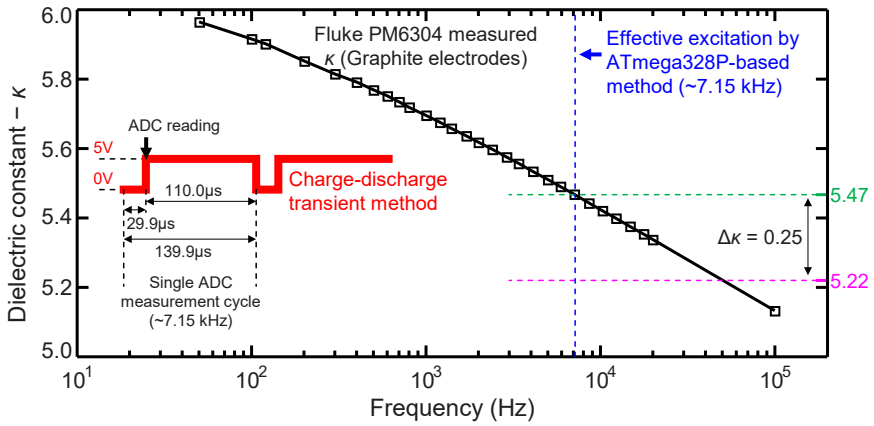

Fig. I.1 Frequency-dependent dielectric constant (κ) of a 22 µm-thick cellulose acetate (CA) sheet with graphite electrodes, measured using a Fluke PM6304 RCL meter. The magenta horizontal line indicates $\kappa = 5.22$, obtained from the global fitting approach by minimizing the Total Sum of Squared Residuals (TSSR) across all electrode materials and CA thicknesses, as shown in Fig. 4(a). The green dashed line marks the measured $\kappa = 5.47$ at the estimated effective probing frequency of ~7.15 kHz, representing this study's ATmega328P-based charge-discharge measurement method. The inset illustrates the transient excitation cycle of the ATmega328P method, highlighting the pulse-driven measurement regime

Section S1: Provides a detailed description of the experimental apparatus setup used for characterizing capacitive sensors in a controlled environment.

Appendix J. Supporting information

Supplementary data associated with this article can be found in the online version at doi:10.1016/j.sna.2025.116779.

Data availability

Data will be made available on request.

References

[1] F. Frasca, A. Caratelli, A. Siani, The capability of capacitive sensors in the monitoring relative humidity in hypogeum environments, IOP Conf. Ser. Mater. Sci. Eng. 364 (2018) 012093, https://doi.org/10.1088/1757-899X/364/1/012093.
[2] R.H. Guy, Handbook of non-invasive methods and the skin, J. Control. Release 42 (1996) 102, https://doi.org/10.1016/0168-3659(96)01365-X.
[3] M.M. Mahmud, J. Li, J.E. Lunsford, X. Zhang, F.Y. Yamaner, H.T. Nagle, O. Oralkan, A low-power gas sensor for environmental monitoring using a capacitive micromachined ultrasonic transducer. in: IEEE SENSORS 2014 Proceedings, IEEE, 2014, pp. 677–680, https://doi.org/10.1109/ICSENS.2014.6985089.
[4] T. Houghton, J. Vanjaria, T. Murphy, H. Yu, Stretchable Capacitive Strain Sensors Based on a Novel Polymer Composite Blend, in: 2017 IEEE 67th Electronic Components and Technology Conference (ECTC), IEEE, 2017: pp. 2263–2268. ⟨https://doi.org/10.1109/ECTC.2017.199⟩.
[5] R. Puers, Capacitive sensors: When and how to use them, Sens Actuators A Phys. 37–38 (1993) 93–105, https://doi.org/10.1016/0924-4247(93)80019-D.
[6] A. Chortos, J. Liu, Z. Bao, Pursuing prosthetic electronic skin, Nat. Mater. 15 (2016) 937–950, https://doi.org/10.1038/nmat4671.
[7] Muneeb-ur-Rahman, G. Shah, A. Ullah, Zia-ur-Rahman, M. Arshad, R. Khan, Zulfiqar, B. Ullah, I. Ahmad, Resistive- and capacitive-type humidity and temperature sensors based on a novel caged nickel sulfide for environmental monitoring, Journal Materials Science Materials Electronics 31 (2020) 3557–3563, https://doi.org/10.1007/S10854-020-02904-Y/TABLES/1.
[8] Y. Pan, M. He, J. Wu, H. Qi, Y. Cheng, One-step synthesis of MXene-functionalized PEDOT:PSS conductive polymer hydrogels for wearable and noninvasive monitoring of sweat glucose, Sens Actuators B Chem. 401 (2024) 135055, https://doi.org/10.1016/j.snb.2023.135055.
[9] J. Min, J. Tu, C. Xu, H. Lukas, S. Shin, Y. Yang, S.A. Solomon, D. Mukasa, W. Gao, Skin-Interfaced Wearable Sweat Sensors for Precision Medicine, Chem. Rev. 123 (2023) 5049–5138, https://doi.org/10.1021/acs.chemrev.2c00823.
[10] R. Matsukawa, A. Miyamoto, T. Yokota, T. Someya, Skin Impedance Measurements with Nanomesh Electrodes for Monitoring Skin Hydration, Adv. Health Mater. 9 (2020) 1–6, https://doi.org/10.1002/adhm.202001322.
[11] F. Ershad, S. Patel, C. Yu, Wearable bioelectronics fabricated in situ on skins, Npj Flex. Electron. 7 (2023) 32, https://doi.org/10.1038/s41528-023-00265-0.
[12] Y. Wang, H. Haick, S. Guo, C. Wang, S. Lee, T. Yokota, T. Someya, Skin bioelectronics towards long-term, continuous health monitoring, Chem. Soc. Rev. 51 (2022) 3759–3793, https://doi.org/10.1039/D2CS00207H.
[13] A.J. Bandodkar, V.W.S. Hung, W. Jia, G. Valdés-Ramírez, J.R. Windmiller, A. G. Martinez, J. Ramírez, G. Chan, K. Kerman, J. Wang, Tattoo-based potentiometric ion-selective sensors for epidermal pH monitoring, Analyst 138 (2013) 123–128, https://doi.org/10.1039/C2AN36422K.
[14] C. Jia, J. Huang, L. Fu, Y. Xiang, Y. Chen, H. Yue, Q. Zhao, W. Gu, Y. Wu, J. Zhang, A Novel Differential Capacitive Humidity Sensor on SIW Re-Entrant Cavity Microwave Resonators With PEDOT:PSS Film, IEEE Sens J. 22 (2022) 6576–6585, https://doi.org/10.1109/JSEN.2022.3155235.
[15] B. Peng, X. Liu, Y. Yao, J. Ping, Y. Ying, A wearable and capacitive sensor for leaf moisture status monitoring, Biosens. Bioelectron. 245 (2024) 115804, https://doi.org/10.1016/j.bios.2023.115804.
[16] F.D.R. Monteiro, P. Stallinga, Using an Off-the-Shelf Lock-In Detector for Admittance Spectroscopy in the Study of Plants, Agric. Sci. 11 (2020) 390–416, https://doi.org/10.4236/as.2020.114023.
[17] AH-304D leaf sensor Rev4 w/clip, (n.d.). ⟨https://biocontrols.com/secure/shop/item.aspx?itemid=134⟩ (accessed November 15, 2024).
[18] M. Thalheimer, A leaf-mounted capacitance sensor for continuous monitoring of foliar transpiration and solar irradiance as an indicator of plant water status, J. Agric. Eng. 54 (2022), https://doi.org/10.4081/jae.2022.1477.
[19] A. Afzal, S.W. Duiker, J.E. Watson, D. Luthe, Leaf Thickness and Electrical Capacitance as Measures of Plant Water Status, Trans. ASABE 60 (2017) 1063–1074, https://doi.org/10.13031/trans.12083.
[20] J.-Q. SUN, X.-Z. ZHAO, C.-Y. LIANG, Z.-X. YANG, Y. LIU, D.-P. QI, The monitoring of plant physiology and ecology: From materials to flexible devices, Chin. J. Anal. Chem. 51 (2023) 100211, https://doi.org/10.1016/j.cjac.2022.100211.
[21] L.M. Ferrari, S. Sudha, S. Tarantino, R. Esposti, F. Bolzoni, P. Cavallari, C. Cipriani, V. Mattoli, F. Greco, Ultraconformable temporary tattoo electrodes for electrophysiology, Adv. Sci. 5 (2018), https://doi.org/10.1002/advs.201700771.
[22] A.J. Bandodkar, W. Jia, J. Wang, Tattoo-based wearable electrochemical devices: a review, Electroanalysis 27 (2015) 562–572, https://doi.org/10.1002/elan.201400537.
[23] X. Zhang, W. Yang, H. Zhang, M. Xie, X. Duan, PEDOT:PSS: from conductive polymers to sensors, Nanotechnol. Precis. Eng. 4 (2021) 045004, https://doi.org/10.1063/10.0006866.
[24] D. Rodrigues, A.I. Barbosa, R. Rebelo, I.K. Kwon, R.L. Reis, V.M. Correlo, Skin-integrated wearable systems and implantable biosensors: a comprehensive review, Biosens. (Basel) 10 (2020), https://doi.org/10.3390/bios10070079.
[25] L.M. Ferrari, U. Ismailov, J.M. Badier, F. Greco, E. Ismailova, Conducting polymer tattoo electrodes in clinical electro- and magneto-encephalography, Npj Flex. Electron. 4 (2020) 1–9, https://doi.org/10.1038/s41528-020-0067-z.
[26] P.M.C. Inácio, R. Guerra, P. Stallinga, An Ultra-Low-Cost RCL-Meter, Sensors 22 (2022) 2227, https://doi.org/10.3390/s22062227.
[27] X. Yue, J. Kiely, R. Luxton, B. Chen, C.N. McLeod, E.M. Drakakis, Passive impedance sensing using a SAW resonator-coupled biosensor for zero-power wearable applications, IEEE Sens J. 22 (2022) 2347–2357, https://doi.org/10.1109/JSEN.2021.3136705.

[28] L.A. Buscaglia, J.P. Carmo, O.N. Oliveira, Simple-Z: a low-cost portable impedance analyzer, IEEE Sens J. 23 (2023) 26067–26074, https://doi.org/10.1109/JSEN.2023.3312039.
[29] A. Al-Ali, A. Elwakil, A. Ahmad, B. Maundy, Design of a Portable Low-Cost Impedance Analyzer, in: Proceedings of the 10th International Joint Conference on Biomedical Engineering Systems and Technologies, SCITEPRESS - Science and Technology Publications, 2017: pp. 104–109. ⟨https://doi.org/10.5220/0006121901040109⟩.
[30] M.W. Widder, L.M. Brennan, E.A. Hanft, M.E. Schrock, R.R. James, W.H. van der Schalie, Evaluation and refinement of a field-portable drinking water toxicity sensor utilizing electric cell–substrate impedance sensing and a fluidic biochip, J. Appl. Toxicol. 35 (2015) 701–708, https://doi.org/10.1002/jat.3017.
[31] S. Grassini, S. Corbellini, E. Angelini, F. Ferraris, M. Parvis, Low-cost impedance spectroscopy system based on a logarithmic amplifier, IEEE Trans. Instrum. Meas. 64 (2015) 1110–1117, https://doi.org/10.1109/TIM.2014.2371191.
[32] S. Grassini, S. Corbellini, M. Parvis, E. Angelini, F. Zucchi, A simple Arduino-based EIS system for in situ corrosion monitoring of metallic works of art, Measurement 114 (2018) 508–514, https://doi.org/10.1016/j.measurement.2016.07.014.
[33] U. Kasiviswanathan, S. Poddar, C. Kumar, S. Jit, S.K. Mahto, N. Sharma, A portable standalone wireless electric cell-substrate impedance sensing (ECIS) system for assessing dynamic behavior of mammalian cells, J. Anal. Sci. Technol. 11 (2020) 25, https://doi.org/10.1186/s40543-020-00223-9.
[34] A. Al-Ali, A. Elwakil, A. Ahmad, B. Maundy, Design of a Portable Low-Cost Impedance Analyzer, in: Proceedings of the 10th International Joint Conference on Biomedical Engineering Systems and Technologies, SCITEPRESS - Science and Technology Publications, 2017: pp. 104–109. ⟨https://doi.org/10.5220/0006121901040109⟩.
[35] Honeywell, Dielectric Constants Lookup Table, (n.d.). ⟨https://prod-edam.honeywell.com/content/dam/honeywell-edam/pmt/hps/products/pmc/field-instruments/smartline-level-transmitters/smartline-guided-wave-level-transmitters/pmt-hps-dielectric-constant-table.pdf⟩ (accessed February 15, 2025).
[36] Clipper Controls, Dielectric Constants of various materials, (n.d.). ⟨https://www.clippercontrols.com/pages/Dielectric-Constant-Values.html⟩ (accessed February 15, 2025).
[37] KAB Electro Acoustics, Dielectric Constants of Common Materials, (n.d.). ⟨https://www.kabusa.com/Dilectric-Constants.pdf⟩ (accessed February 7, 2025).
[38] Dixon, Dielectric Constants, (n.d.). ⟨https://canada.dixonvalve.com/sites/default/files/documents/dielectric-constant-values_0.pdf⟩ (accessed February 7, 2025).
[39] Goodfellow, Cellulose Acetate Film, (n.d.). ⟨https://www.goodfellow.com/eu/cellulose-acetate-film-1000001942⟩ (accessed February 7, 2025).
[40] A. Wagner, H. Kliem, Dispersive ionic space charge relaxation in solid polymer electrolytes. I. Experimental system polyethylene oxide, J. Appl. Phys. 91 (2002) 6630–6637, https://doi.org/10.1063/1.1468911.
[41] D.J. Bonthuis, S. Gekle, R.R. Netz, Profile of the static permittivity tensor of water at interfaces: consequences for capacitance, hydration interaction and ion adsorption, Langmuir 28 (2012) 7679–7694, https://doi.org/10.1021/la2051564.
[42] K. Chang, G.M. Geise, Dielectric permittivity properties of hydrated polymers: measurement and connection to ion transport properties, Ind. Eng. Chem. Res 59 (2020) 5205–5217, https://doi.org/10.1021/acs.iecr.9b03950.
[43] J. Lee, L.G. Kaake, J.H. Cho, X.-Y. Zhu, T.P. Lodge, C.D. Frisbie, Ion gel-gated polymer thin-film transistors: operating mechanism and characterization of gate dielectric capacitance, switching speed, and stability, J. Phys. Chem. C. 113 (2009) 8972–8981, https://doi.org/10.1021/jp901426e.
[44] M. Samet, V. Levchenko, G. Boiteux, G. Seytre, A. Kallel, A. Serghei, Electrode polarization vs. Maxwell-Wagner-Sillars interfacial polarization in dielectric spectra of materials: characteristic frequencies and scaling laws, J. Chem. Phys. 142 (2015), https://doi.org/10.1063/1.4919877.
[45] A. Olivares, I. Cosme, S. Mansurova, A. Kosarev, H.E. Martinez, Study of electrical conductivity of PEDOT:PSS at temperatures >300 K for hybrid photovoltaic applications, in: 2015 12th International Conference on Electrical Engineering, Computing Science and Automatic Control (CCE), IEEE, 2015: pp. 1–3. ⟨https://doi.org/10.1109/ICEEE.2015.7357906⟩.
[46] Z. Khurelbaatar, K.-H. Shim, J. Cho, H. Hong, V.R. Reddy, C.-J. Choi, Temperature dependent current-voltage and capacitance-voltage characteristics of an Au/n-Type Si schottky barrier diode modified using a PEDOT:PSS Interlayer, Mater. Trans. 56 (2015) 10–16, https://doi.org/10.2320/matertrans.M2014263.
[47] R. Hampson, G. Dobie, Steady state physical modeling for optimizing capacitive tactile sensors thermal sensitivity, IEEE Sens J. 23 (2023) 26047–26054, https://doi.org/10.1109/JSEN.2023.3315969.
[48] H. Park, S.H. Lee, F.S. Kim, H.H. Choi, I.W. Cheong, J.H. Kim, Enhanced thermoelectric properties of PEDOT:PSS nanofilms by a chemical dedoping process, J. Mater. Chem. A 2 (2014) 6532–6539, https://doi.org/10.1039/C3TA14960A.
[49] Y. Feldman, A. Andrianov, E. Polygalov, I. Ermolina, G. Romanychev, Y. Zuev, B. Milgotin, Time domain dielectric spectroscopy: An advanced measuring system, Rev. Sci. Instrum. 67 (1996) 3208–3216, https://doi.org/10.1063/1.1147444.
[50] Y. Sun, J. Pang, Y. Han, W. Guo, Z. Li, A method for studying the transient dielectric behavior of nonlinear insulating dielectrics based on combined measurement of current and open-circuit potential, Measurement 249 (2025) 117024, https://doi.org/10.1016/j.measurement.2025.117024.
[51] E. Jung, C.-S. Park, T. Hong, H.-S. Tae, Structure and dielectric properties of poly (vinylidenefluoride-co-trifluoroethylene) copolymer thin films using atmospheric pressure plasma deposition for piezoelectric nanogenerator, Nanomaterials 13 (2023) 1698, https://doi.org/10.3390/nano13101698.
[52] J.M. Mativetsky, J. Tarver, X. Yang, B.E. Koel, Y.-L. Loo, Structural origin of anisotropic transport in electrically conducting dichloroacetic acid-treated polymers, Org. Electron 15 (2014) 631–638, https://doi.org/10.1016/j.orgel.2013.12.019.
[53] J. Alam, X. Xu, P.C.O. Adu, Q. Meng, K. Zuber, S. Afshar, H.-C. Kuan, J. Ma, Enhancing thermoelectric performance of PEDOT: PSS: A review of treatment and nanocomposite strategies, Adv. Nanocomposites 1 (2024) 16–38, https://doi.org/10.1016/j.adna.2023.08.001.
[54] H. He, J. Ouyang, Enhancements in the mechanical stretchability and thermoelectric properties of pedot:pss for flexible electronics applications, Acc. Mater. Res 1 (2020) 146–157, https://doi.org/10.1021/accountsmr.0c00021.
[55] T. Kim, S. Park, J. Seo, C.W. Lee, J.-M. Kim, Highly conductive PEDOT:PSS with enhanced chemical stability, Org. Electron 74 (2019) 77–81, https://doi.org/10.1016/j.orgel.2019.06.033.

Pedro Inácio received his Integrated Master's degree (2013) and Ph.D. (2023) in Electronic and Telecommunications Engineering from the University of Algarve, Portugal. His doctoral research focused on developing ultra-low-noise sensors for detecting bioelectrical signals in various biological systems, including non-electrogenic cell populations and embryoid bodies derived from cardiomyocytes, small organs, and cancerous tissues. In 2024, he began a postdoctoral position at the Center for Electronics, Optoelectronics, and Telecommunications (CEOT), Portugal, where his research has been centered on developing capacitive sensor technology for real-time monitoring of plant physiological health.

Rui Guerra graduated in Physics (1991), MSc in Nuclear Physics (1995; area of Particle Physics), both from the Faculty of Sciences of the University of Lisbon, and PhD in Physics from the IST, Technical University of Lisbon (1999; area of Plasma Physics). In 2000, he was a post-doc at the Laser Physics Group at the University of Umeå, Sweden, in Laser Spectroscopy. He joined the University of Algarve in 1996 as a lecturer and became an Assistant Professor in 2000. His current interests include light scattering and absorption in biological media and their application to the non-destructive measurement of fruit tissue properties. Another related area is the detection of fruit physiopathologies by optical means, e.g., fluorescence and, more recently, electrical measurements.

Peter Stallinga graduated in Physics (1988), PhD in Physics of electronic materials from the University of Amsterdam, Netherlands (1994). He joined the University of Algarve in 1997 as a PostDoc, became a lecturer in 1999, and an Assistant Professor in 2000. His interests include electrical characterization of semiconductor defects through magnetic resonance, organic electronics, sensing, electronic instrumentation, and biotechnology.